Large-scale Dynamics of Perceptual Decision Information across Human Cortex

Niklas Wilming[1*], Peter R Murphy[1], Florent Meyniel[2], Tobias H Donner[1,3,4,5*]

[1]Section Computational Cognitive Neuroscience, Department of Neurophysiology and Pathophysiology, University Medical Center Hamburg-Eppendorf, Martinistrasse 52, Hamburg 20251, Germany

[2] University Paris-Saclay, Inserm, CEA, NeuroSpin, Cognitive Neuroimaging Unit, 91191, Gif-sur-Yvette, France

[3]Bernstein Center for Computational Neuroscience, Charité Universitätsmedizin, Haus 6, Philippstraße 13, 10115, Berlin, Germany

[4]Department of Psychology, University of Amsterdam, Weesperplein 4, 1018 XA, Amsterdam, The Netherlands

[5]Amsterdam Brain and Cognition, University of Amsterdam, Nieuwe Achtergracht 129, 1018 WS, Amsterdam, The Netherlands

*Corresponding authors

Abstract

Perceptual decisions entail the accumulation of sensory evidence for a particular choice towards an action plan. An influential framework holds that sensory cortical areas encode the instantaneous sensory evidence and downstream, action-related regions accumulate this evidence. The large-scale distribution of this computation across the cerebral cortex has remained largely elusive. We developed a regionally-specific magnetoencephalography decoding approach to exhaustively map the dynamics of stimulus- and choice-specific signals across the human cortical surface during a visual decision. Comparison with the evidence accumulation dynamics inferred from behavior enabled us to disentangle stimulus-dependent and endogenous components of choice-predictive activity across the visual cortical hierarchy. The endogenous component was present in primary visual cortex, expressed in a low (< 20 Hz) frequency-band, and its time course tracked, with delay, the build-up of choice-predictive activity in (pre-)motor regions. Our results are consistent with choice-specific cortical feedback signaling in a specific frequency channel during decision formation.

Introduction

A fundamental issue in neuroscience is to understand the mechanisms underlying decisions about the state of the sensory environment. Convergent progress in computational theory, behavioral modeling, and neurophysiological analysis has converged on an influential framework for perceptual decisions: Sensory evidence supporting a particular choice is accumulated over time into an internal "decision variable"; in many contexts, this decision variable is reflected in the motor plan to report the corresponding choice [1–4]. Computational models based on these notions perform well in fitting behavioral choice, reaction times, and associated confidence, of different species in a variety of behavioral task protocols [4–6]. Specifically, when the duration of available perceptual evidence is controlled by the environment, the sign of the decision variable at the end of the evidence sequence determines choice, and its magnitude [7,8], combined with elapsed time [9], determines the associated confidence.

The above class of models affords an intuitive interpretation of neural signals that have been observed at different processing stages of the cerebral cortex of several species. The sensory evidence relevant for a given choice task is encoded by sensory cortical neurons [10]. For example, neuronal populations in

visual cortical area MT encode the net direction of random dot motion patterns [11,12] and neuronal populations in area V4 encode the dominant color of these patterns [12]. By contrast, neural correlates of accumulated sensory evidence have been identified in the build-up of motor preparatory activity in different regions of the rat [13], monkey [2,3,9,14], and human cerebral cortex [15–18]. These results are in line with the idea that sensory responses are fed into an integrator on their way to associative and (pre-) motor cortical circuits [2,19,20].

Yet, the large-scale cortical organization of perceptual decision computations has remained elusive, for a number of reasons. First, only few studies have assessed the dynamics of sensory and choice-related neural signals across multiple cortical areas [12,21–23]. Second, such large-scale neural dynamics have not been related to the time course of evidence accumulation inferred from behavior – which is, in turn, critical for their computational interpretation [24–26]. Third, the above framework entails a purely feedforward accumulation of sensory evidence across the cortical sensory-motor pathways. In this view, decision-related neural activity in sensory cortex only reflects the feedforward impact of sensory evidence on choice [11,27]. By contrast, the large-scale network implementing the transformation from sensory input to choice is equipped with powerful feedback connections from association and (pre)-motor cortex to sensory cortex [28,29]. In hierarchical circuit models of decision-making, these feedback connections continuously propagate the evolving decision variable from downstream regions to sensory regions [25,26]. As a consequence, the choice-predictive activity observed in sensory cortical areas should be a mixture of a stimulus-dependent (feedforward) and an endogenous (feedback) component [25,26]. Recent single-unit results from monkey visual cortex are consistent with such decision-related feedback [30–32], but the source of this feedback remains unknown.

Identifying the neural implementation of perceptual decision-making requires an integrated behavioral and large-scale physiology approach. Controlled fluctuations in momentary sensory input are instrumental for inferring the time course of evidence accumulation from behavior, and for pinpointing the nature of decision-related neural signals [4,13,25,26]. Specifically, they help un-mix stimulus-dependent and putative endogenous components of choice-predictive neural activity [30], within different stages of the sensory cortical hierarchy.

Here, we developed such an integrated approach in the human brain. We combined a visual perceptual choice task with behavioral analysis of the underlying evidence accumulation dynamics and a novel, atlas-based, regionally-specific MEG decoding technique. This enabled us to concurrently track the dynamics of (i) sensory evidence weighting on behavioral choice, (ii) the encoding of the instantaneous as well as accumulated stimulus information, and (iii) decision build-up across the mosaic of functional regions spanning the cortical surface. Taken together, this approach illuminated the nature of decision-related signals across human cortex.

Results

Our task required participants (N=15) to compare the mean contrast of a "test stimulus" with the contrast of a previously presented "reference stimulus" that was constant across trials (Figure 1A and Methods for details). The stimuli were circular gratings spanning the entire projection screen (radius > 10° of visual angle) and expanded or contracted on a given trial (no changes of direction within trials). The reference contrast was 50% on all trials. The test had a mean contrast that was stronger or weaker than the reference contrast (stimulus category randomly chosen per trial; mean continuously adjusted to 75% accuracy through a staircase procedure). Critically, the test was made up of a stream of ten "samples" (100 ms each) with contrast levels that fluctuated around the mean contrast for the trial, requiring participants to accumulate the fluctuating contrast values over time in order to compute their mean. The test stimulus offset prompted participants to deliver their behavioral report by button press. They responded with the left or right hand to report "test stronger" or "test weaker" choices and with the index or middle finger to indicate high or low confidence about the accuracy of that choice, respectively.

Temporal profile of evidence weighting for behavioral choice

A number of observations indicate that participants indeed accumulated contrast information across the complete test stimulus interval (i.e., all ten samples, Figure 1B, Figure S1). First, participants' choices were reliably predicted by mean test contrast in all participants (mean prediction accuracy: 76%, range 61-81%; stratified 5-fold cross-validated logistic regression), and their confidence judgments lawfully depended on average test contrast, exhibiting signatures established in other tasks [8,33] (Figure S1A-C).

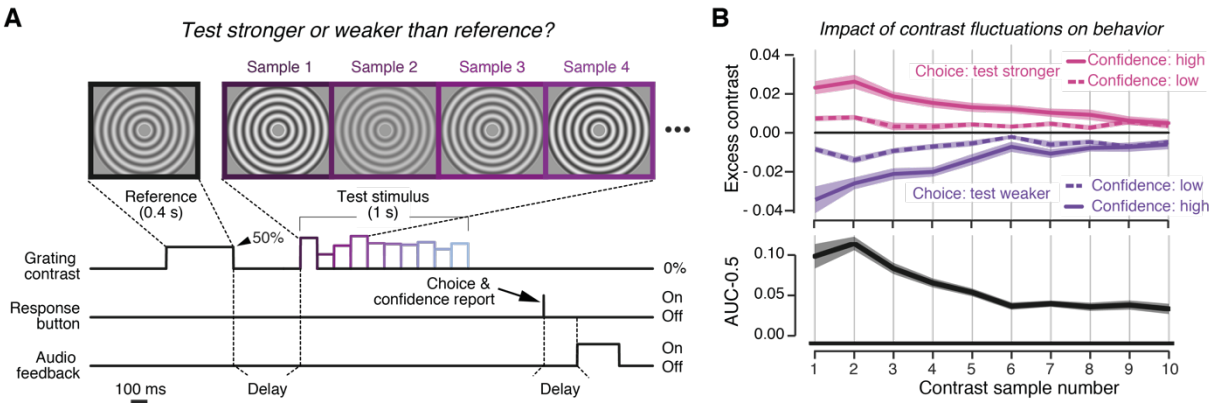

Figure 1. Behavioral task and temporal accumulation of sensory input for decision-making. A. Schematic of task events during example trial. Each trial started with a "reference" stimulus, a circular moving (expanding or contracting) grating with constant contrast (50% in all trials), followed (1-1.5 s delay) by a "test" stimulus. The test was another circular moving grating made up of ten consecutive samples of fluctuating contrast. Sample contrasts were drawn from a normal distribution (Methods). The task was to indicate if the mean test contrast (averaged across samples) was stronger or weaker than the reference contrast. Auditory feedback (low or high tone) was provided after another variable delay (0-1.5 s). Gratings depicted here have lower spatial frequency than in the experiment for visualization purposes. **B.** Impact of contrast fluctuations on behavior. Top, contrast fluctuations around the sample mean ($\pm\mu_s$, i.e. expected contrast on sample s) sorted by behavioral response (choice and confidence judgment); error bars ±SEM. Bottom, psychophysical kernel quantifying impact of trial-by-trial contrast fluctuations on choice, as a function of sample position, expressed as deviation of area under the ROC-curve from chance level (AUC=0.5, see Methods). Gray shading, SEM; horizontal bar, $p < 0.05$ (FDR-corrected two-sided t-test of AUC different from 0.5). Source data are provided as a Source Data file.

Second, contrast information at all sample positions had a significant leverage on behavior (Figure 1B). Contrast fluctuations affected both choice (Figure 1B, top; compare curves for "test stronger" vs. "test weaker" choices) as well as confidence reports (compare "high confidence" vs. "low confidence" for the same choice). We used psychophysical reverse correlation [30,34–36] to quantify the time course of the weighting of contrast information on choice. The evidence weighting time courses, so-called psychophysical kernels, were computed as the area under curve (AUC) of the receiver-operating characteristic relating a given contrast level to the participant's choice ([37]; see Methods for details). The AUC ranged between 0 and 1, whereby values of 0.5 indicated chance level. AUC-values for all sample positions were significantly larger than 0.5 (Figure 1B, bottom), indicating that sample contrasts stronger than reference tended to be followed by "test stronger" choices. Critically, however, the impact of contrast samples on choice declined over time across the test stimulus interval (Figure 1B, bottom; slope of psychophysical kernel: -0.009, $t(14)=-5.3$, $p=0.0001$). This is consistent with results from a range of other perceptual choice tasks in humans and monkeys [34–36,38], and provides a reference for interpreting the dynamics of decision-related neural activity below.

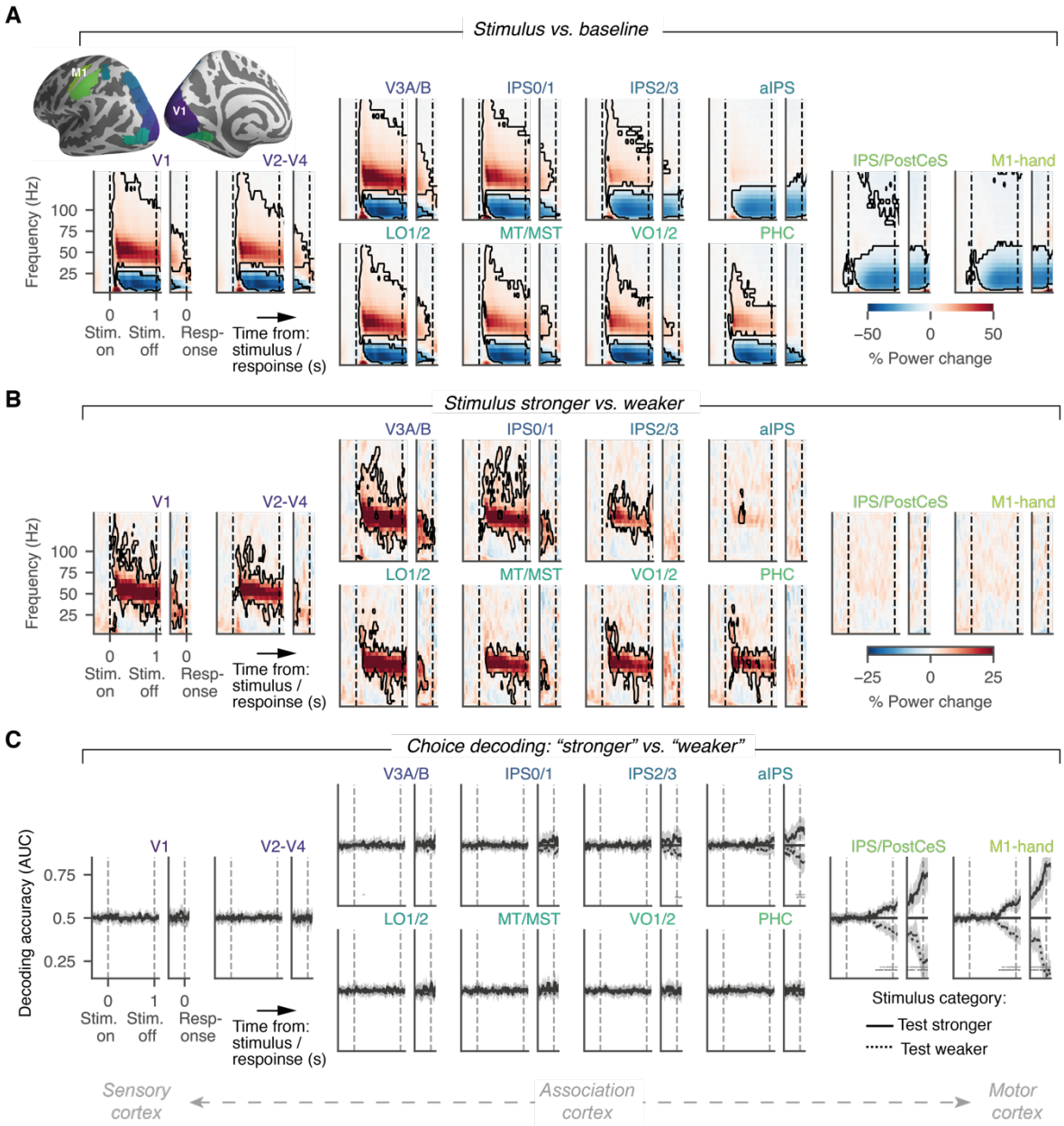

Figure 2. Task-related neural dynamics across the visuo-motor cortical pathway. **A.** Time-frequency representations (TFRs) of group average power change relative to pre-stimulus baseline (-250 to 0 ms relative to test stimulus), for several cortical regions along the cortical sensory-motor axis. Top left inset, colors of areas depicted on cortical surface. For each area, data are shown time-locked to test stimulus-onset in the left partition of each TFR and time-locked to the choice, in the right partition (partitions separated by white spacing). Black contour, $p<0.05$ (cluster-based permutation test against 0). **B.** As A, but for power differences between stronger and weaker test stimulus categories. **C.** Time courses of regionally-specific decoding of choices (see Methods), separately for the two test stimulus categories. Gray shading, 95% highest density interval; horizontal bars, $p<0.05$ (cluster-based permutation test: AUC different from 0.5). Source data are provided as a Source Data file.

Sensory encoding across the visual cortical hierarchy

We reconstructed the dynamics of sensory and decision-related activity in many cortical regions (Methods). We focused on a set of fMRI-defined regions that are implicated in the visuo-motor decision process for detailed characterization of the properties of the physiological signals reflecting sensory input and ensuing decision (Figure 2 and Methods). This set consisted of multiple topographical maps of the visual field (see Methods for area labels) and three regions exhibiting hand movement-specific lateralization: anterior intraparietal sulcus (aIPS), the junction of the IPS and postcentral sulcus (IPS/PostCeS), and the hand-specific sub-region of primary motor cortex (henceforth called "M1-hand"). In complementary analyses, we tracked sensory and decision-related activity (through decoding of spectral and spatial patterns) in a set of 180 regions per hemisphere covering the entire cortex (Figure 3 and Methods).

Previous work has shown that population activity in visual cortex scales monotonically with stimulus contrast in a high frequency range, including the gamma-band (about 40-70 Hz) [39–45]. Correspondingly, the power in a narrow band gamma-band (45-65 Hz), as well as a broader high-frequency band (65 to about 120 Hz, "high-frequency"), was elevated relative to pre-stimulus baseline (Figure S2A) throughout stimulus presentation, in all visual field maps, but not in the movement-selective regions (Figures 2A and S2B). By contrast, alpha-/beta-band (about 8-36 Hz) activity was suppressed during the test stimulus in all areas, including the movement-selective ones (Figures 2A and S2B). The power responses in the gamma- and high frequency-bands, but not in alpha- and beta-bands, also differentiated between trials with stronger and weaker test contrast (Figures 2B and S2C), thus reflecting the two mean stimulus categories judged by the participants.

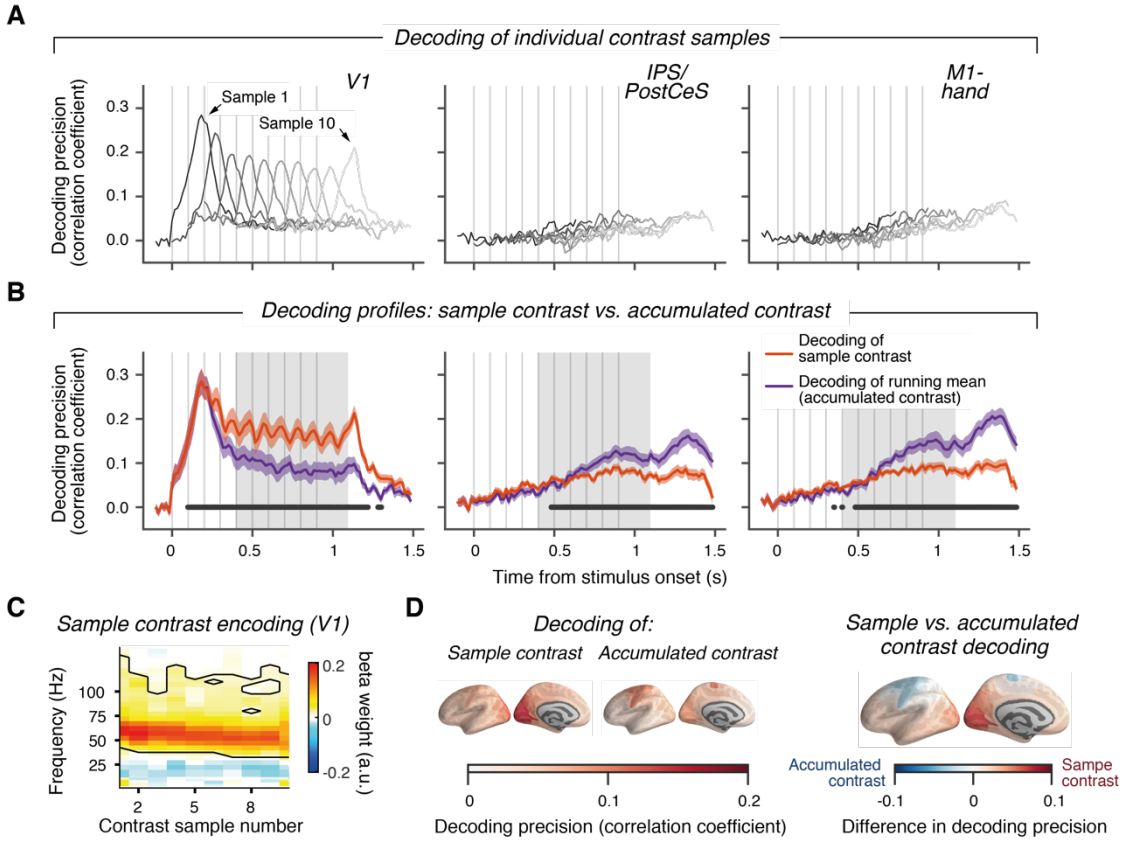

Figure 3: Decoding of contrast and accumulated contrast across cortex. A. Time courses of frequency-based (range: 1-145 Hz; V1: averaged across hemispheres, IPS/PostCeS/M1-hand: lateralized power values) decoding of single-trial contrast values, separately for each sample position, from V1 (left), IPS/PostCeS (middle) and M1-hand (right) power responses. Decoding precision is expressed as cross-validated Pearson correlation coefficient between decoded and presented contrast (see Methods). **B.** Decoding of sample contrast and of running mean of contrast. Orange lines, convex hull across decoding peaks for individual samples in panel A. Magenta lines, convex hull across decoding time courses for the running means of sample contrast values up to sample $i \in \{1, \ldots, 10\}$. This reflects the neural representation of the decision-relevant quantity in the task. Orange/magenta shading, SEM; horizonal bar: $p<0.05$ (cluster-based permutation test of decoding of sample contrast vs. decoding of accumulated contrast). **C.** Encoding of individual contrast samples as a function of frequency; black contour, $p<0.05$ (cluster-based permutation test). **D.** Decoding precision (convex hull averaged across gray shaded areas in B) for all ROIs: Single contrast samples (left), accumulated contrast (center) and their difference (right). Source data are provided as a Source Data file.

Power responses in the gamma- and high frequency-bands decayed monotonically during test stimulus presentation (Figure S2B, C), with a slope that depended on the variance of sample-to-sample contrast fluctuations (Fig S3; V1: $F(2,28) = 3.92$, $p = 0.03$, 1-way ANOVA). This observation is in line with an attenuating effect of contrast adaptation on visual cortical responses observed in previous work [46]. Critically, this decay of visual cortical responses, at least in part, explained the decay in evidence sensitivity throughout the trial that was evident in behavior: the individual time courses of gamma- and high frequency-band power were strongly correlated with the time courses of psychophysical kernels (Figure S4).

Responses in the gamma- and high-frequency bands also specifically tracked the rapid sample-to-sample contrast fluctuations throughout the trial (Figures 3). We trained pattern classifiers to decode sample contrast from local spectral patterns (power values from 1-145 Hz) and correlated decoded with physical sample contrasts (Methods). Contrast decoding profiles in V1 for consecutive samples peaked about 190 ms after sample onset (Figure 3A). The convex hull curve of peak decoding values for individual contrast samples, a summary measure of decoding performance across samples, was significantly better than chance throughout decision formation (Figure 3B, orange). Just like the gamma-band and high-frequency responses, the precision of V1 contrast decoding also decreased monotonically from the first to the ninth sample (Figure 3B left), tracking the decay of overall gamma-band and high-frequency responses (Figure S5). A complementary "encoding analysis" (using frequency-resolved regressions assuming predominantly linear encoding of contrast in MEG power, see Methods and Discussion), confirmed that the gamma-band contributed most to the contrast decoding in V1: regression weights were strongest in the gamma-band and significant only for the gamma- and high frequency-bands (Figure 3C). In sum, neural population responses in V1 and extrastriate visual cortical areas conveyed detailed information about the sample-to-sample contrast fluctuations, which was specifically contained in the gamma- and high frequency-bands.

Encoding of action plan and accumulated evidence in the cortical visuo-motor pathway

When choices are reported with left- or right-hand movements (as in our task), the hemispheric lateralization of activity in motor and parietal cortical regions encodes specific choices [15,47,48]. This activity is frequency-specific and builds up during decision formation [15,16,49], evident in the power lateralization (contra- vs. ipsilateral to effector choice) of M1-hand in our data (Figure S6A). Correspondingly, decoders trained on the spectral power profiles from both hemispheres revealed choice-predictive build-up activity in M1-hand as well as IPS/PostCeS (Figure 2C). Choice decoding in these regions ramped up more quickly before choices associated with high than with low confidence (Figure S6B).

Choice-predictive activity in IPS/PostCeS was partially independent of M1-hand: When eliminating signal leakage by removing M1-hand power from IPS/PostCeS power for each frequency (via linear regression), the residual IPS/PostCeS activity still yielded significant choice decoding (AUC=0.53, time=1.1 s; $t(14)=2.01$, $p=0.032$). Movement-specific activity in IPS/PostCeS has previously been observed with fMRI during perceptual choice [48], but the build-up of activity in this region during evidence accumulation, prior to overt behavioral choice, has not yet been established.

The above analyses focused on a set of cortical regions, in which the format of choice-predictive activity in terms of motor preparatory activity is well understood (see above and Figure S2). Two complementary analyses applied the same choice decoding approach as for Figure 2C to 180 regions spanning the entire cortical sheet (Figure S7A), as well as an alternative choice decoding approach (using more fine-grained spatial information as well as signal phase and amplitude, Methods) to a set of pre-selected frontal regions based on previous work (Figure S7B). This showed the strongest choice-predictive activity in motor cortex (M1 and PMd) supporting our focus on action-related regions (see Discussion).

Activity in motor and parietal cortex (M1 and IPS/PostCeS, respectively) tracked not only the evolving plan to act (choice-predictive activity), but also the ongoing computation of the decision-relevant quantity: the mean of contrast samples. We trained pattern classifiers to decode the running mean of contrast samples at a specific latency after sample onset (dubbed "accumulated contrast" in Figure 3; see Methods). The correlation between the decoded and actual accumulated (running mean of) contrast quantified the precision of accumulated contrast read-out from spectral activity ("accumulated contrast", magenta lines in Figure 3B). Decoding values late in the trial (after gray box) were likely affected by the hand movement execution, but movement execution could not explain decoding before 1.1 s after stimulus onset: Our analyses excluded reaction times faster than 1.225 s and used a maximum time window of 250 ms for spectral estimation; thus, 1.1 s corresponded to the fastest reaction time minus half the spectral estimation time window. Also note that the observed decoding of accumulated contrast should be considered a lower bound on the expression of the hypothetical decision variable in cortex:

the analysis assumed perfect accumulation of all contrast samples across time, so any deviation from this assumption (e.g., due to reduction in evidence sensitivity, Figure 1B) reduced decoding precision.

Mapping the sensitivity of neural responses to instantaneous or accumulated contrast (average of convex hulls across the interval 0.4 to 1.1 s, gray box in Figure 3B) across the cortical surface also showed strongest decoding of individual contrast samples for early and intermediate visual cortical areas (with peak reliability in V1), whereas decoding of accumulated contrast prevailed in the same action-related regions of parietal and (pre-)motor cortex (Figure 3D), in which build-up activity also predicted behavioral choice (compare Figure S7A). Overall, the functional properties of IPS/PostCeS, PMd, and M1 activity resembled those of monkey and rodent parietal and frontal cortical regions during similar perceptual choice tasks [2,13,14]. Mapping the dynamics of stimulus- and choice-encoding across the cortical surface yielded results in line with the idea that the action plan encoded in these parietal and frontal cortical regions was computed by accumulating the contrast samples over time.

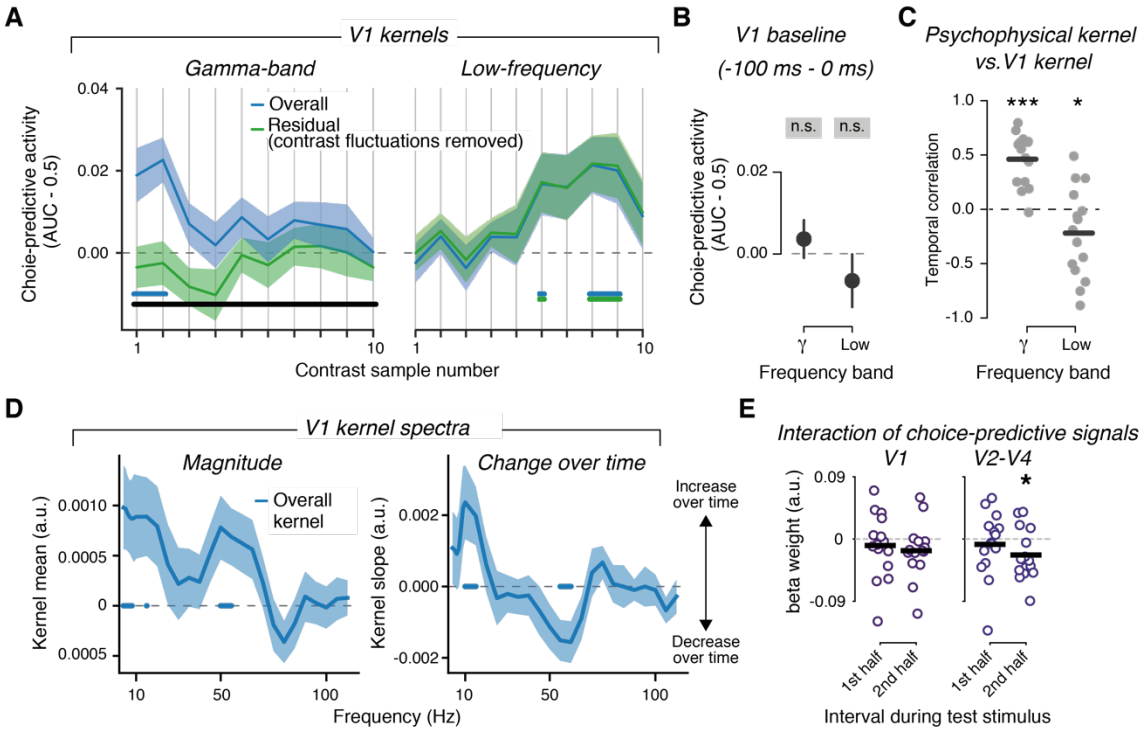

Figure 4. Dissociating stimulus-driven and endogenous components of choice-predictive signals in V1. A. Kernels quantifying the impact of hemisphere-averaged V1 power fluctuations (within each test stimulus category) on behavioral choice ("V1 kernels") for V1 activity in the gamma-band (40-75 Hz, left) and low-frequency (0-20 Hz right). Power values have been extracted at the latency of peak contrast encoding (t=190 ms from sample onset). Blue, "overall kernels" based on all fluctuations in V1 power. Green, "residual kernels" for fluctuations after removing effect of external stimulus fluctuations (see main text). **B.** Test for choice-predictive gamma-band and low-frequency activity during pre-stimulus baseline interval. **C.** Correlation of V1 kernels with psychophysical kernel from Fig. 1B. Each dot is one participant. Black lines, group average. **D.** Frequency spectra of choice-predictive activity in V1. Left, kernels collapsed across time. Right, change of kernels across test stimulus interval (slope across samples). **E.** Interaction of impact of low-frequency and gamma-band activity on behavioral choice, for areas V1 and V2-V4. All error bars and shades, SEM. All p-values from t-tests. Horizontal bars, p<0.05 (colored bars, difference from 0; black bars, difference between blue and green). * p < 0.05, **; p<0.01; *** p<0.001. Source data are provided as a Source Data file.

Untangling choice-predictive activity in visual cortex

We next sought to investigate the dynamics of choice-predictive activity in more detail for visual cortical areas. The temporal profile of choice-predictive activity in sensory cortex, combined with the temporal profile of sensory evidence weighting (i.e., psychophysical kernel), can help "reverse-engineer" decision-related interactions between processing stages involved in evidence encoding and evidence accumulation, respectively [25,26]. This choice-predictive activity refers to the trial-to-trial correlation between neural activity fluctuations within a stimulus category and behavioral choice. It is commonly dubbed as "choice probability" for single-unit activity, yielding small but significant values for early visual cortex [11,27,30,50]. We quantified this activity in the same way as psychophysical kernels, but

replacing sample contrast with the band-limited power in different visual cortical areas (Methods). While this analysis is analogous to the one used to calculate single-unit choice probabilities, we refer to the resulting measure as "V1 kernels" to highlight the difference to single-unit spiking activity (see Discussion).

Visual cortical gamma-band responses encoded the fine-grained contrast information (Figures 2B, 3) that subjects used for solving the task (Figures 1, S1). We thus reasoned that choice-predictive fluctuations of gamma-band activity should mirror the impact of visual contrast information on choice inferred from behavior (Figure 1C). Indeed, V1 gamma-band kernels (40-75 Hz, range based on Figure 2B) were larger than zero (i.e., AUC>0.5) early in the trial (Figure 4A, left, "overall kernels" in blue, $p<0.05$ for samples 1 and 2 only), but neither during the baseline interval before the test stimulus (Figure 4B, left; $t(14)=-1.24$, $p=0.24$), nor late in the trial (Figure 4A). V1 gamma-band kernels decayed over time (group average slope: -0.017, $t(14)=-3.1$, $p=0.007$) just like the psychophysical kernels, yielding a highly significant temporal correlation (Figure 4C, left; group average correlation: $r=0.45$, $t(14)=6.5$, $p=1.3\times10^{-5}$).

In circuit models with feedback from the accumulation stage, choice probabilities in sensory cortex reflect a mixture of feedforward and feedback components [25,26]. These components can be disentangled by removing the contribution of stimulus fluctuations to neural activity [25,30]. If choice-predictive activity fluctuations reflect the impact of external stimulus fluctuations on choice, removing the stimulus-induced fluctuations should reduce (or even cancel) the correlation between neural activity and choice [25]. This is exactly what we found for V1 gamma-band activity: The "residual kernels" (computed after removal of contrast fluctuations via linear regression, see Methods) did not differ from zero (green in Figure 4A, left; $p>0.05$ for all sample positions) and overall kernels (blue) were consistently larger than the residual kernels (green) for all sample positions (Figure 4A, left, black bar).

V1 choice-predictive activity in the low frequency range (0-20 Hz) was markedly different from the choice-predictive activity in V1 gamma-band (Figure 4A, right, blue). Trial-to-trial fluctuations in V1 low-frequency power also predicted choice variability, but only for later samples (Figure 4A), and not during the pre-stimulus baseline (Figure 4B; right; $t(14)=-1.32$, $p=0.21$). Accordingly, the time courses of V1 low-frequency kernels and psychophysical kernels were *negatively* correlated (Figure 4C, right; group average correlation: $r=-0.23$, $t(14)=-2.19$, $p=0.045$; difference to gamma-band: $t(14)=5.88$, $p=0.00005$). What is more, removing contrast-driven fluctuations from low-frequency power did not change the magnitude and shape of V1 low-frequency kernels (Figure 4A, right, green). Thus, the choice-predictive fluctuations in low-frequency power resulted from endogenous sources, rather than from the external stimulus. Similar results were found across the visual cortical hierarchy (Figure S8). In sum, choice-predictive fluctuations of low-frequency and gamma-band activity dissociated in terms of both their temporal profiles (primacy vs. recency) and sources (external stimulus vs. internal).

To delineate the spectral profiles of the above-described effects, we also analyzed choice-predictive activity across a broad frequency range as a function of frequency. Indeed, overall choice-predictive activity (collapsed across samples) was confined to the low-frequency and gamma-bands (Figure 4D, left), and the kernel slope (i.e., change over time) showed an *increase* in V1 kernel magnitude over sample positions, specifically for the alpha-band (around 10 Hz, center frequency for computation of low-frequency kernels) and a *decrease* in the gamma-band (Figure 4D, right). Thus, the functional dissociation between different components of decision-related V1-activity was expressed in clearly delineated frequency bands.

While having dissociated functional properties, endogenous and stimulus-dependent choice-predictive activity components, in low-frequency and gamma-bands respectively, might interact, somewhere in the visual cortical hierarchy. To test this possibility, we jointly regressed power in these two bands on behavioral choice (logistic regression, Methods). We quantified the decaying vs. increasing temporal profiles for both bands, as the asymmetry of beta weights between first and second halves of the test stimulus interval. In line with the opposite kernel slopes in our more fine-grained analysis from Figure 4D, we found opposite temporal profiles of choice-prediction regression coefficients in both bands (Figure S9). Critically, an interaction term included in the regression was negative for the second half

of the decision interval in V2-V4 (Figure 4E; t(14)=-2.4, p=0.0305). There was a similar trend in V1: t(14)=-1.6, p=0.127). This suggests that low-frequency activity suppressed the impact of early visual cortical gamma-band responses on choice towards the end of decision formation, when the choice-predictive low-frequency activity in visual cortex was particularly strong.

Association between choice-predictive activity in visual cortex and downstream regions

The choice-predictive activity evident in V1 low-frequency power might reflect recurrent dynamics within visual cortex and/or feedback of decision-related signals from downstream regions outside of the visual system [25,26]. The build-up of the group average time course of V1 low-frequency kernels (Figure 4A, right) resembled the build-up of choice-predictive activity in downstream regions (Figure 2C), consistent with the feedback scenario. To quantify this relationship, at the level of individual subjects, we re-computed visual cortical low-frequency kernels at the same temporal resolution as downstream choice decoding signals (Figure S10) and correlated the time courses, for a range of different time lags (see Figure 5, top left inset and Methods). For all early visual field maps (V1 and V2-V4), the group average cross-correlations were robust for M1 leading (but not following) visual cortex (Figure 5, black bars) with a peak lag of 150 ms.

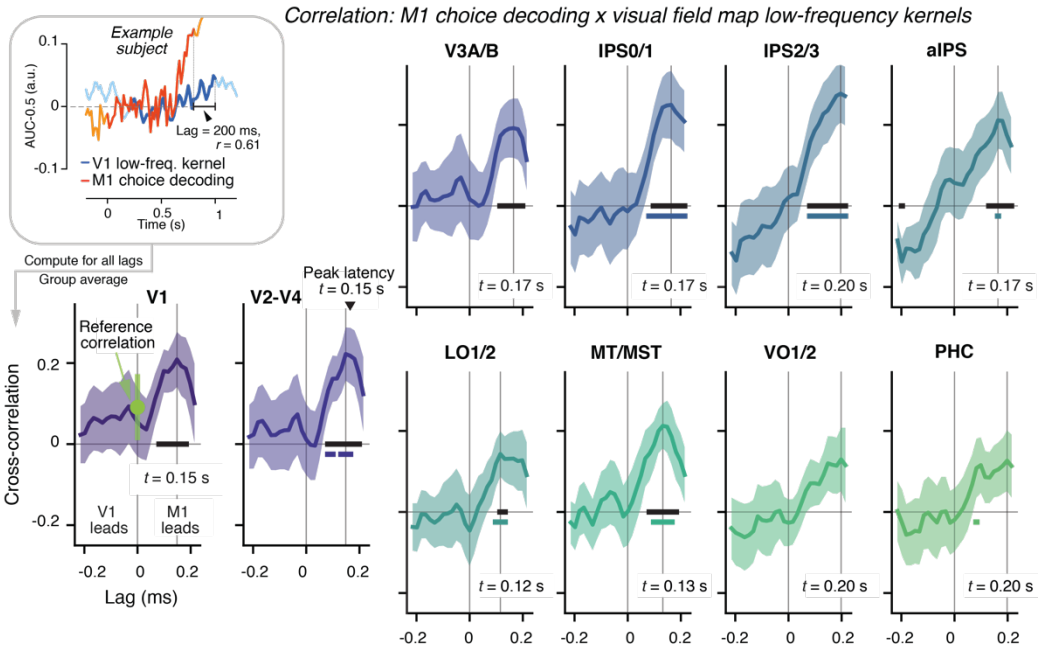

Figure 5. Cross-correlation between choice-predictive activity in downstream regions and low-frequency kernels across visual cortical field maps. Cross-correlation between M1-hand accumulated contrast profile (Figure 3B, right) and V1 (overall) low-frequency kernel re-computed at the same temporal resolution (Figure S10). Inset. Illustration of analysis approach for one example subject and lag. We computed the cross-correlation function between V1 low-frequency kernel and choice-predictive M1 activity for a range of lags from -215 to 215 ms (positive lags indicating lead of M1 choice signal), and then averaged across subjects. Reference correlation is correlation between choice-predictive activity and low-frequency kernel at lag t=0, both taken from M1 (upper bound of signal leakage); it is shown in V1 plot (green) but was applied to evaluate correlations for all visual field maps. All error bars and shades, SEM. Horizontal bars, p<0.05 (t-tests). Black bars: test against 0; colored bars: test against reference correlation. Source data are provided as a Source Data file.

The positive, non-zero peak lags are consistent with feedback and argue against signal leakage as the source of the correlation. As a reference for leakage, we quantified the zero-lag correlation between choice-predictive activity and low-frequency kernel, now both taken from M1 (Figure 5, green data point on top of M1-V1). This "reference correlation" constituted an upper bound of the leakage that might have been present in the estimates of areas other than M1, thus overestimating the true leakage component present in the visual field map data. Despite the conservative nature of this reference, the cross-correlations with visual cortex at positive lags were significantly larger for several field maps including V2-V4 (Figure 5, colored bars). These results indicate that the cross-correlations for visual field maps reflect genuine coupling between choice-predictive neural signals in motor and visual cortex.

The cross-correlations observed here do not necessarily reflect direct (mono-synaptic) interactions between choice-predictive activity in (pre-)motor regions and the visual cortical areas (other areas might have relayed the signals). Our results also do not rule out a contribution of interactions within visual cortex to the choice-predictive low-frequency fluctuations in V1 and other visual cortical areas. Even so, our results show that decision-related visual cortical activity in the low-frequency closely tracked the build-up of decision-related activity in downstream brain regions involved in action preparation.

Discussion

The neurobiology of perceptual decision-making has witnessed considerable advances in the integration between computational theory and both physiological and psychophysical experimentation [1,2]. The dominant neurobiological framework of perceptual decision-making (but see [22,51,52]) entails the sustained accumulation of transient sensory signals encoded in sensory cortex on the way to association and motor cortex, leading to the gradual build-up of an action plan. Largely due to technical challenges, this framework has so far lacked a detailed characterization of this dynamical computation across the large mosaic of interconnected regions of the primate cortex. In particular, the framework has ignored the role of abundant feedback connections from association and (pre-)motor regions to sensory cortex.

Here, we developed an approach for tracking the dynamics of stimulus- and choice-related information across human cerebral cortex. In an elementary decision task that entailed the accumulation of visual contrast information over time, we found a predominant involvement of early visual cortex in evidence encoding and a predominant involvement of parietal as well as (pre-) motor regions in evidence accumulation and action planning. We also found a spectral multiplexing of stimulus-dependent and endogenous components of choice-predictive activity fluctuations in visual cortical population activity: The stimulus-dependent component was expressed in the gamma-band, and the endogenous component in low (<20 Hz) frequencies, peaking in the alpha-band. The latter tracked the build-up of choice-information in the downstream regions involved in action planning.

Our current insights hinged on the ability to track the time course of the encoding of sensory evidence, accumulated evidence, and action plan, from each of a large set of well-delineated cortical regions. To this end, we combined atlas-based MEG source reconstruction with a multivariate pattern classification approach that was based on the *spectro-spatial* patterns of local activity within each region. Previous electrocorticography work on brain-computer interfaces has highlighted such spectro-spatial patterns as useful features for pattern classification [53]. Current fMRI approaches enable decoding of sensory or cognitive variables from fine-grained multi-voxel patterns in multiple cortical regions [54–57], but they lack the necessary temporal resolution for tracking the dynamics of decision formation. Conversely, E/MEG decoding studies [58–60] provide the critical temporal resolution, but commonly use the whole sensor array as features for decoding, precluding inferences about the information flow between brain regions. Being situated between these two classes of approaches, our current approach provides the opportunity to track large-scale information dynamics across cortical areas, analogous to recent animal work [12,21,23,61]. In contrast to these large-scale physiology studies in animals, however, we here quantified the associations between regionally-specific information dynamics and the psychophysically-inferred time course of evidence accumulation. This, in turn, constrained their functional interpretation.

Complementary analyses indicated that choice information in anterior intraparietal (IPS/PostCeS) and (pre-) motor cortical regions was primarily contained in large-scale spatial biases (right vs. left hemisphere) with respect to the action (left vs. right hand button press) prepared to report the choice (Figure S6A). Indeed, decoding based on the spectral patterns of lateralization yielded very similar results as in Figure 2C (see source data file). We found no robust choice encoding in regions that did not exhibit such large-scale biases. When using finer-grained spatial patterns of both signal phase and amplitude as features for decoding, we did not find strong choice-predictive activity in more anterior regions of prefrontal cortex, even though this yielded higher choice-prediction values for M1 than the coarser-grained approach (Figure S7, compare panels B and A, see Methods for all differences). Previous studies have identified action-independent, choice-predictive signals in human prefrontal cortex during tasks, in which the perceptual choice could not be mapped onto a specific action plan

during decision formation [12,56,62]. Our task, however, allowed for such a mapping, mimicking a large body of work in animals [2,13,14,23]. The locus and format (action-dependent vs. -independent) of cortical build-up activity during decisions depends on the task context [63]. In our task, the build-up activity may have been exclusively expressed in the format of motor preparatory activity. Even so, it is possible that M1 hand area and IPS/PostCeS only reflected the outcome of an evidence accumulation process that took place elsewhere (e.g., the striatum [19]), which we failed to detect with our approach.

Our decoding approach was agnostic about the nature and specifics of the neural code used for solving the task [64]. We assume that the decision process reads out the spiking output of visual cortical activity, rather than the amplitude of local field potential fluctuations, including oscillations in the gamma-band [41]. V1 spiking activity also scales with contrast in a monotonic fashion, and is generally closely coupled to local field potentials (and the resulting MEG activity) in the gamma-band [45]. But both signals can dissociate [65]. For example, power and peak frequency scale approximately linearly with contrast across the full range [40,41,44,65], whereas V1 spiking saturates at high contrasts [66]. By exploiting the full spectral (and spatial) pattern of power changes, both peak shifts and amplitude changes could be used for visual contrast decoding, rendering our approach generic and robust.

Limitations of our analyses, as well as possible, genuine dissociations between the decoded signal and the decision-relevant neural code, may have caused an underestimation of the true link between visual cortical activity and behavioral choice. Specifically, endogenous (stimulus-independent) fluctuations in the neural stimulus-representation that is "read out" in the decision should impact behavioral choice [64]. However, we did not detect such a choice-predictive effect in the residual V1 gamma-band activity. Our analysis attempted to estimate these endogenous fluctuations by removing, via linear regression, trial-to-trial variations in gamma-band activity explained by the physical contrast. This was based on the assumptions that (i) MEG power scaled approximately linearly with contrast and (ii) stimulus-related and endogenous components superimpose linearly. Both assumptions are simplified: contrast response functions in MEG power may not be perfectly linear in all individuals (see [67] for demonstration for motion coherence response functions), and recent work indicates that stimulus- and choice-related cortical signals, instead, interact multiplicatively [68]. Consequently, caution is warranted when interpreting the absence of a choice-predictive component in residual V1 gamma-band activity observed in our analysis (Figure 4): It may reflect technical limitations, such as a failure of our linear approach to isolate the endogenous gamma-band fluctuations and/or the generally low signal-to-noise ratio of MEG gamma-band activity [45]. Alternatively, or in addition, this may be due to gamma-band activity being only an indirect proxy of the neural code used for the decision computation.

Our results highlight the utility of decomposing the local field potential into different frequency bands for disentangling distinct components of cortical computation. The results also add to the mounting evidence for the co-existence of stimulus-related and endogenous components in the choice-predictive activity of visual cortex [25,30], and they provide new physiological markers that can also be assessed in the frequency-specific field potential activity from invasive animal data as well from hierarchical cortical circuit models. While spectral analysis helped to disentangle the stimulus-related and endogenous component of activity, we do not conceptualize these two frequency-specific signals as independent entities. There is abundant evidence for interactions between power in different frequency bands, including alpha and gamma, in the cortex [45,69]. For the choice-predictive power components assessed here, we found a negative multiplicative interaction between the impact of low-frequency and gamma-band activity on choice in areas V2-V4 (Figure 4F). These choice-specific cross-frequency interactions should be further characterized by means causal interventions.

Our findings also add to the realization that adaptation phenomena in sensory cortex likely contribute to decision-making [4,22]. Attenuation of sensory responses is a well-established phenomenon in various behavioral states (including anesthesia), which has been explained in terms of local micro-circuit properties [46,70,71]. Yet, most models of perceptual choice have ignored adaptation. In our task, we found a progressive attenuation of visual cortical gamma-band responses, dependent on sample variance. This progressive attenuation predicted the individual reduction in the impact of evidence on choice evident in psychophysical kernels. Such primacy in psychophysical kernels has often been explained by bounded evidence accumulation at the decision stage [34,36]. In line with ref [22] (their Figure 2e), our results

indicate that the attenuation of neural responses at sensory processing stages can account, at least in part, for a decrease in evidence sensitivity over time. Note that both mechanisms, bounded accumulation and adaptation, are not mutually exclusive, but might, in fact, interact in the presence of decision feedback.

The observation that stimulus-dependent and endogenous components of decision-related activity in early visual cortex were expressed in the (high-frequency and) gamma-band vs. the low-frequency (alpha) band, respectively, resonates with an emerging view of the role of the gamma- and alpha-bands in message passing across the cortical hierarchy. In this view, feedforward and feedback information flow through the cortical hierarchy is mediated by layer-specific pathways communicating in these two spectral channels, respectively [29,39,72–76]. Those studies have quantified the properties of physiological local field potentials recorded from different areas (e.g. time-lagged correlations between regions or laminar activity profiles within regions), without a link to specific behaviors. The functions of these cortical feedforward and feedback pathways have been conceptualized in the context of attention [77] and predictive coding [73,78], but not the accumulation of evidence towards a choice. Evidence accumulation, the essence of dynamic belief updating, may provide a powerful framework for advancing and testing theories of frequency-specific channels for inference. Our current insights suggest that the spectral profiles of the associated local field potential activity (our MEG source estimates) help disentangle the feedforward and feedback components of decision-related signals in the cortical hierarchy. Future work should assess if, and to what extent, the contribution of gamma-band activity to the feedforward signaling of decision-relevant sensory evidences generalizes to stimuli beyond contrast gratings, which induce strong, narrow-band gamma oscillations (see above). Recent results from a visual evidence accumulation task entailing small checkerboard patches flashed at different positions suggest they do [79].

Another important issue for future work is to pinpoint the function of decision-related feedback to early visual cortex during evidence accumulation. Feedback signals may be the source of confirmation biases [26], a pervasive feature of human perceptual and higher-level judgment [80]. In natural environments, the source of the sensory evidence can change unpredictably [81–84]. Such volatile environments might provide deeper insight into the adaptive function of decision-related feedback signals.

Acknowledgments
We thank Stanislas Dehaene, Mariano Sigman, and Genis Prat Ortega for discussion during this project, and Klaus Wimmer and Alan Stocker for thoughtful comments on the manuscript. This work has been funded by the Deutsche Forschungsgemeinschaft (DFG, German Research Foundation), grants DO 1240/3-1, DO 1240/4-1, and SFB 936 - Projekt-Nr. A7 (all to T.H.D).

Author contributions
NW: Conceptualization, Methodology, Investigation, Software, Formal analysis, Visualization, Writing – original draft, Writing – review and editing; PRM: Conceptualization, Methodology, Writing – review and editing; FM: Conceptualization, Writing – review and editing; THD: Conceptualization, Methodology, Resources, Writing—original draft, Writing—review and editing, Supervision.

Methods

Participants
Fifteen participants (8 female, 7 male) participated in the experiment. All had normal or corrected to normal vision and no history or indications of psychological or neurological disorders. The experiment was approved by the ethics committee of the Medical Association Hamburg. Participants gave written and informed consent. Each participant completed one training session and four recording sessions in the MEG. Sessions were spread out over several days and were typically completed within 10 days. We also collected a structural MRI for each participant in a separate session, unless an MRI scan was available from previous experiments. Participants were paid 10 € per hour.

Task and procedure
Participants completed five different recording sessions and each session consisted out of five blocks à 500 trials, lasting approximately 60 minutes. The first session was a training session used for exposing

participants to the task and to calibrate their performance to 75% correct. A trial consisted of the following sequence of events (Figure 1A). First, a reference stimulus (grating of fixed contrast at 0.5) was displayed for 400 ms. After a variable delay (uniform between 1 and 1.5 s) ten successive samples of variable contrasts (see below) were shown (each 100 ms); together these ten samples made up the test stimulus, the mean contrast of which participants should compare with the reference (i.e. forced choice: "stronger than reference" or "weaker than reference").

The offset of the last sample marked the beginning of the response period for participants. Participants reported their binary choice, and their confidence about the correctness of that choice ("high" vs. "low") simultaneously, by pressing one of four different buttons, whereby the two hands were always mapped to different choices (choice-to-hand mapping counterbalanced across participants). The index and ring fingers of each hand were then used to report confidence (again mapping counterbalanced across participants). During MEG sessions, participants used two response pads, one for each hand. During the training sessions participants, used the same stimulus-response mapping, but pressed keys on a computer keyboard. After a participant's response and a consecutive variable delay between 0 and 1.5 s auditory feedback was given (250 ms duration). A low tone indicated a wrong answer and a high tone indicated a correct answer.

The ten consecutive contrast samples were draws from a normal distribution centered on a participants 75% accuracy contrast level. This threshold was determined by running a QUEST staircase [85] continuously in the background. The standard deviation of the normal distribution was chosen randomly from [0.05, 0.1, 0.15] from trial to trial. After each set of 100 trials participants could take a short break self-timed break. After the third block, participants took a longer break lasting at least five minutes.

Stimuli

We used expanding or contracting circular gratings similar to the stimuli from Michalareas [39]. The intensity of a given pixel was given by computing a blending value for each pixel:

$$a_{(x,y)} = \frac{1}{2} + \frac{1}{2}\sin\left(\frac{d_{(x,y)} - s}{2r\pi}\right), \tag{1}$$

where $d_{(x,y)}$ was the distance of pixel (x,y) to the center of the screen and r=3/4° determined the spatial frequency of the grating. Varying s over frames yielded expanding or contracting gratings, respectively. We varied s such that the grating moved with a speed of 4/3 °/s. On each trial, the grating either expanded or contracted, but never changed direction. To obtain a final color value we used $a_{(x,y)}$ to blend two grayscale colors that had the desired contrast:

$$l_{(x,y)} = a_{(x,y)}\left(0.5 - \frac{c}{2}\right) + \left(1 - a_{(x,y)}\right)\left(0.5 + \frac{c}{2}\right), \tag{2}$$

where c was the desired contrast. We furthermore set an inner annulus with a radius of 1.5° to uniform gray. Gratings had a generative radius of 12.5°, but were truncated by the vertical screen border at a radius of 11.3°. The contrast of the reference grating was always set to 0.5, while the contrast of the test stimulus varied and changed every 100 ms, as controlled by the staircase procedure (see above).

Stimuli were generated using Psychtoolbox 3 for Matlab. They were back-projected on a transparent screen using a Sanyo PCL-XP51 projector with a resolution of 1920 x 1080 at 60 Hz. The luminance profile was linearized by measuring and correcting for the systems gamma curve. A doubling of contrast values therefore also produced a doubling of luminance differences. During the first training session stimuli were presented on a VIEWPixx monitor with the same resolution and refresh rate (also linearized).

Data acquisition

We used a CTF MEG system with 275 axial gradiometer sensors and recorded at 1200Hz. Recordings took place in a dimly lit magnetically shielded room. We concurrently collected eye-position data with a SR-Research EyeLink 1000 eye-tracker (1000Hz). We continuously monitored head position by using three fiducial coils. After seating the participant in the MEG chair, we created and stored a template head position. At the beginning of each following session and after each block we guided participants

back into this template position. We used Ag/AgCl electrodes to measure ECG and vertical and horizontal EOG.

Data analysis

Evaluation of choice and confidence dependence on contrast
We used a logistic regression to evaluate whether participants exploited different contrast samples for their choices and confidence judgements. We fit the following logistic regression to predict choices from contrast values:

$$y_{trl} = logistic\left[\sum_{i\in\{1..10\}} \beta_i c_{trl,i} + \beta_0\right], \quad (3)$$

where y_{trl} was the choice in a given trial and $c_{trl,i}$ the contrast value of sample i in the same trial. We evaluated the accuracy of this fit with 5-fold cross-validation. All available trials from one subject were split into five folds and we used each fold as test set once and all remaining folds for weight estimation. We carried out cross validation per subject and then averaged across folds and subjects. Since we titrated participants' accuracy to 75% correct, we also expected that the accuracy of this logistic regression is bounded close to 75% correct. We also evaluated whether confidence judgements were based on contrast. To this end, we fit a similar logistic regression, but this time predicted confidence judgements for each response separately. We again evaluated the accuracy of this logistic regression with 5-fold cross-validation.

Definition of trial categories for the current task
The computation of psychophysical kernels described below required sorting trials into four categories defined by a unique combination of the physical stimulus category (i.e. mean contrast of test stimulus stronger or weaker than reference) and the participant's perceptual choice (test "stronger" or "weaker"). We defined these four categories based on signal detection-theory [37], as follows. Hits and misses: "stronger" and "weaker" choices, respectively for trials in which the physical test stimulus was stronger than the reference; false alarms and correct rejects: "test stronger" and "test weaker" choices, respectively for trials in which the physical test stimulus was weaker than the reference.

Computation of psychophysical kernels
With the term "psychophysical kernel", we refer to the time course of the correlation between trial-to-trial fluctuations in stimulus sample contrast and the participant's behavioral choice, after factoring out the physical stimulus category (i.e., mean test contrast stronger or weaker than reference). Psychophysical kernels were computed by comparing single-trial sample contrast values at a given sample position, between both behavioral choices, within a given stimulus category (test contrast stronger or weaker than reference). To this end, we computed the receiver-operator-characteristic curve (ROC), separately for each stimulus category and sample position, and from this the area under the ROC curve. The resulting AUC values (range: 0-1) quantified the predictive power of contrast fluctuations around their mean level within a stimulus category for choice. AUC values of 0.5 indicated that contrast fluctuations did not differ between choices, whereas AUC values of 1 indicated perfect separation of contrast values between choices. We computed separate AUC time courses by comparing (i) hits and misses and (ii) false alarms and correct rejects. The resulting two AUC time courses were averaged, yielding the single psychophysical kernel shown in Figure 1C.

Preprocessing, spectral analysis, and source reconstruction of MEG data
We used beamforming to reconstruct the sources of activity observed at the MEG sensor level. First, we automatically labeled artifacts in raw MEG data by detecting blinks, muscle artifacts, sensor jumps and cars passing by in the vicinity of the building. Blinks were detected based on concurrently recorded eye-movement signals (SR-Research EyeLink 1000). Sensor jumps were detected by convolving each sensor with a filter designed to detect large sudden jumps and subsequently by looking for outliers in the filter response. Muscle and environmental artefacts were detected by filtering each channel in the 100-140Hz or <1Hz range and by detecting outliers that occurred simultaneously in many channels. To remove

power line noise, we applied a notch filter. In a final step, we epoched data, downsampled to 600Hz and discarded all epochs that contained artifacts.

We computed time-frequency representations (TFRs) of single-trial data by using a multi-taper method. For low frequencies (1-9Hz in steps of 1Hz), we used a window length of 0.25 s (frequency smoothing of 8Hz). For high frequencies (10-150Hz in steps of 5Hz), we used a window length of 0.1 s (20Hz frequency smoothing).

We used linearly constrained minimum variance (LCMV) beamforming to estimate activity time courses at the level of cortical sources [86]. We constructed individual three-layer head models from subject specific MRI scans using fieldtrip ([87]; functions, ft_volumesegment and ft_prepare_mesh). Head models were aligned to the MEG data by a transformation matrix that aligned the average fiducial coil position in the MEG data and the corresponding locations in each head model. Transformation matrices were generated using MNE software [88]. We computed one transformation matrix per recording session. Third, we reconstructed cortical surfaces from individual MRIs using Freesurfer and aligned two different atlases to each surface [89,90]. In a fourth step we used MNE [88] to compute LCMV filters for projecting data into source space. LCMV filters combined a forward model based on the head model and a source space constrained to the cortical sheet (4096 vertices per hemisphere, recursively subdivided octahedron) with a data covariance matrix estimated from the cleaned and epoched data. We computed one filter per vertex, based on the covariance matrix computed on the time-points from stimulus onset until 1.35s after stimulus onset across all trials. We chose the source orientation with maximum output source power at each cortical location. In a final step, we computed TFRs of the epoched MEG data (same method as described for the sensor-level TFR decomposition) and projected the complex time series into source space. In source space we computed TFR power at each vertex location and then averaged across all vertices within a ROI. We aligned the polarity of time-series at neighboring vertices, because the beamformer output potentially included arbitrary sign flips for different vertices.

For all analyses except the one for Figure S7B, we collapsed power values within hemisphere-specific regions of interest across vertices. We then converted the power values into units of percent power change (i.e., modulation) relative to the baseline power in each frequency [15]. To this end, we averaged power estimates across trials and time in a pre-stimulus interval (-250 to 0 ms before test stimulus onset). This yielded a frequency-specific, but condition-independent, baseline that was applied to normalize power values from each trial. The baseline was computed by averaging across all vertices within each hemisphere-specific part of a given region of interest (ROI; see below). For Figure S7B (fine-grained decoding), no pre-trial baseline was necessary due to feature standardization during the decoding analysis.

For all analyses except for Figures 2C and S7, the resulting baseline corrected hemisphere-specific power modulation values were collapsed or subtracted across hemispheres. The subtraction yielded the hemispheric lateralization of power modulations between the hemisphere contralateral and ipsilateral to the hand used to report "test stimulus is stronger" (choice-to-hand mapping counterbalanced across participants, see section *Task and Procedure* above).

Cluster	Functional areas	Source
V1	Dorsal and ventral part of V1	Ref. [89]
V2-V4	Dorsal and ventral parts of V2, V3, V4	
V3A/B	V3A, V3B	
IPS0/1	IPS0, IPS1	
IPS2/2	IPS2, IPS3	
Lateral occipital	LO1, LO2	
MT+	TO1, TO2	
Ventral occipital	V01, V02	
PHC	PHC1, PHC2	
aIPS	aIPS1	Ref. [48]
IPS/PostCeS	IPS/PostCeS	
M1 (hand)	M1	

Table 1: *ROI definition along the sensorimotor pathway.*

Regions of interest

We used two sets of ROIs. The first was confined to 18 cortical regions, all of which were defined by previous fMRI work and co-registered to individual structural MRIs: (i) retinotopically organized visual cortical field maps described in the atlas from Wang et al. [89] and (ii) three regions exhibiting hand movement-specific lateralization of cortical activity: aIPS, IPS/PCeS and the hand sub-region of M1 [48]. Following a scheme proposed by Wandell and colleagues [91], we grouped retinotopic visual cortical regions with a shared foveal representation into clusters (see Table 1), thus increasing the spatial distance between ROI centers and minimizing the risk of signal leakage. The second, cortex-wide, set of ROIs were 180 regions covering the cerebral cortex, as defined in [90]. Those we also co-registered to individual MRIs.

Choice-specific lateralization of spectral power

We computed TFRs of choice-specific power lateralization for each ROI (contralateral vs. ipsilateral to hand movement used to report "test stronger" choice). Lateralized activity was computed for each physical stimulus (i.e. mean test contrast) and choice condition separately before computing the final contrast that isolated choice-specific activity. For the latter, we contrasted error and correct responses for each physical stimulus (contrast) condition separately. We first averaged trials from each combination of stimulus and choice condition and subsequently computed the difference between hits and misses, and then the difference between false alarms and correct rejects, and finally averaged these two differences. In other words, we computed the difference between "test stronger" and "test weaker" choices, separately for each physical stimulus condition (mean contrast of test stimulus), and only averaged their results afterwards. This ensured that any activity differences due to the physical stimulus were factored out and the result isolated differential activity that was specific to behavioral choice. When computing choice-specific power changes on hemisphere- averaged power values, we found no significant effects in any ROI (data not shown). Statistical significance of lateralization values was assessed by cluster-based permutation test (threshold free cluster enhancement, H=2, E=0.5, $p<0.05$).

Stimulus-specific (test contrast-related) dynamics of spectral power

Stimulus-specific activity was computed similarly to the above choice-specific activity, but on TFRs of the hemisphere-averaged power values (not their lateralization). This was done because the full-field, centrally presented visual grating stimuli were expected to produce about equally strong sensory responses in both hemispheres. To factor out choice information in this analysis, conversely to the computation of choice-specific activity, we now contrasted different physical stimulus conditions (i.e., mean test contrast), separately for each choice and then averaged their result. Statistical significance of power changes was assessed by cluster-based permutation test (TFCE, H=2, E=0.5, $p<0.05$).

Decoding of choices

We used multivariate pattern classification techniques [92] to decode choice information contained in the estimated activity patterns of individual ROIs. Decoding was carried out separately for each time point throughout the trial in order to generate time courses of choice-predictive activity.

We used three different choice decoding approaches, referred to as approaches (i), (ii), and (iii) below. These approaches differed in their spatial extent and granularity as well as in the treatment of the two stimulus categories (i.e., "test contrast stronger than reference" and "test contrast weaker than reference"). Approaches (i) and (ii) used the spectral pattern of power values (1-145 Hz) from both hemispheres for each ROI (i.e. coarse-grained spatial patterns), and we trained separate classifiers per stimulus category, effectively asking the classifiers to separate correct choices from errors within stimulus category. Thus, decoders from approaches (i) and (ii) could exploit hemisphere-and frequency-specific power values from each time point and stimulus category to predict choices. In both approaches, features were z-scored before decoding based on training data only, and the same transformation was applied to test data before evaluating decoding performance. We used linear support vector machines for decoding (C=1). Since choices were not equally distributed (<p_yes> = 0.57, <crit> = -0.23), we up sampled the minority class in the training data (but not in the test set) by randomly repeating elements

until the frequency of choices was equal. In approach (i), the above-described procedure was applied to the visuo-motor pathway set of ROIs (Figure 2C). In approach (ii), this procedure was applied to the cortex-wide set of ROIs (Figure S7A).

Approach (iii) used the spectral patterns of phase and power values from each individual vertex (fine-grained spatial patterns) for a subset of ROIs from the above two sets (Figure S7B). Due to the high computational demand of approach (iii), we focused it on M1-hand (for comparison) and 17 pre-selected ROIs in dorsolateral prefrontal cortex anterior to premotor cortex, which have been implicated in different aspects of decision-making by previous work [5]. The procedure was as described above, except that we trained only one decoder to predict choices across both stimulus categories, and that we performed dimensionality reduction after z-scoring. The latter was done due to the large number of features: two (power and phase) per vertex and frequency bin. We first computed principle components of the training set and kept all components that cumulatively explained 95% of the variance of the training set. We then projected training and test set data into the space defined by these components. We then evaluated a linear support vector machine with *L1* penalty (C=10/number of features) and discarded all features whose weights were below 1e-5. Finally, we trained another support vector machine (*L2 penalty*) on the final reduced feature set (C=1/2) and plotted the performance of this classifier on the test set (Figure S7B). Principal component analysis and feature selection were performed exclusively on the training set and then applied to the test set.

In all three approaches, we evaluated decoding performance by means of 10-fold cross-validation and computed ROC-AUC values to evaluate each classifier and averaged across folds. We split all data per subject into ten folds, keeping the same percentage of choices in each fold. We then used nine folds to determine parameters of the classifier and computed prediction scores on the tenth fold, which we used to compute ROC-AUC values. We used Bayesian inference to estimate uncertainty around average decoding performance (error bars in Figure 2B). We assumed that a participants AUC value (subscript s below) at time point t were samples from a T distribution, here ignoring boundedness of AUC values because values were far from the bound, and placed weakly informative priors on all parameters of this distribution. We obtained posterior estimates using pymc3 [93]:

$$auc_{s,t} = StudentT(\mu_t, \sigma_t, \gamma), \tag{4}$$

$$\mu_t \sim \mathrm{N}(0.5, 1), \tag{5}$$

$$\sigma_t \sim U(0, 5), \tag{6}$$

$$\gamma \sim Exp\left(\frac{1}{29}\right) + 1, \tag{7}$$

We used the NUTS sampler and two MCMC chains with 3000 iterations. We checked convergence visually and by ensuring that $\hat{R}$ was below 1.05. Uncertainty estimates in Figure 2B display the 95% highest density interval for μ_t.

We also compared decoding values in IPS/PostCeS after accounting for linear relationships with activity in M1-hand. We repeated decoding in IPS/PostCeS using single trial power values across all frequencies. But this time we first predicted IPS/PostCeS power values from their corresponding values in M1-hand using linear regression for each frequency separately. We subtracted this prediction from IPS/PostCeS power values and repeated the decoding procedure as before.

Decoding of sample contrast or running mean of sample contrast ("accumulated contrast")

We used a regression approach to assess whether source reconstructed spectral activity tracked individual contrast samples or the running mean of contrast samples (termed "accumulated contrast" in Figure 3). Because the test stimulus was large and spanned both visual hemifields, we reasoned that decision-relevant neural activity in retinotopic areas should, likewise, span both hemisphere-specific parts of the visual field maps. Thus, individual contrast samples should be decodable from hemisphere-averaged activity in visual cortical field maps. Because choice-predictive activity in downstream (pre-) motor regions was primarily contained in the hemispheric lateralization of power values contra- vs-ipsilateral to the upcoming hand movement, we further assumed that the decision-relevant quantity, the running mean of contrast samples, should also be decodable from lateralized activity in choice related areas. We, therefore, used either hemisphere-averaged power values from 1-145 Hz, lateralized power

values (contralateral vs. ipsilateral to hand movement used to report "test stronger" choice) for the results shown in Figure 3.

In a separate analysis approach, we used separate power values from each hemisphere-specific part of each ROI for decoding of sample contrast or its running mean. This allowed the decoders to combine information from both hemispheres and use either the mean across hemispheres or the lateralization if beneficial. We found that this yielded almost identical results to those shown in Figure 3, with very strong correlations of the decoding time courses (e.g., average correlations across subjects: 0.95 for decoding of sample contrast from V1; 0.91 for decoding of accumulated contrast from M1-hand). Decoding of accumulated contrast using lateralized power values yielded slightly better decoding performance (t-test at t=1.3s, peak for decoder that used both hemispheres separately: p=0.0003, t=4.67) presumably because the classifier had fewer but equally informative features at its disposal. Given that our choice to average or lateralize hemispheres was theoretically motivated from the outset and gave marginally better results, we decided to present the more constrained decoding results.

For each ROI, time point *t* and subject we extracted single trial power values for all frequencies within the range from 1-145 Hz. We used hemisphere hemisphere-averaged or lateralized power at each time point *t* to predict the contrast of each sample *i* ($i \in \{1..10\}$), or the running mean of contrast samples up to sample *i*, called accumulated contrast. This yielded one prediction per trial, contrast sample position, time-point, subject, region of interest and hemisphere combination (averaged or lateralized).

We used ridge regression to predict target values (sample contrast or accumulated contrast). Power values were z-scored based on training data only and the same transformation was applied to test data before evaluating prediction performance. The analysis yielded the linear combination of frequency-specific power values that maximized the correlation between predictors and response variable (current sample contrast or accumulated contrast). The strength of L2 regularization applied by ridge regression was governed by a single parameter which we optimized in a nested cross-validation (possible values were 0.1, 1, 10). We evaluated prediction performance by computing the Pearson correlation between predicted contrast and actual contrast. To decode the running mean of all contrast samples (accumulated contrast), we averaged the true contrast of all preceding and the current sample (i.e. up to sample i), assuming perfect evidence accumulation for simplicity, and predicted this value using the same power values. We used 10-fold cross-validation in all cases (see above for more details).

Encoding of sample contrast (regression)
We also used linear regression to assess the sensitivity of activity at distinct frequencies to sample contrast. For this "encoding" analysis, we isolated single-trial power fluctuations at 190 ms after the onset of each contrast sample (identified as the peak latency of sample contrast decoding in the previous analysis), and for each frequency *f* and sample position *i* fit the following regression model:

$$p_{trl,i,f} = \beta_1 c_{trl,i} + \beta_0, \tag{8}$$

where *p* denotes power and *c* denotes sample contrast, both of which were normalized (z-scored) prior to fitting. The fitted coefficients β_1 reflect the strength and direction of the relationship between frequency-specific power and sample contrast, and are shown for V1 in Figure 3C (similar results were found for other visual field maps, data not shown). The reliability of time- and frequency-resolved contrast encoding at the group level was assessed via cluster-based permutation test.

Neural-activity kernels
We computed "neural-activity" kernels analogously to psychophysical kernels to quantify choice-information contained in different frequency bands and ROIs. Kernels were computed by substituting single-trial sample contrast values with frequency and ROI specific power values, again for both contrast conditions separately ("test larger than reference" and "test lower than reference").

To maximize sensitivity for small-amplitude choice-predictive signals, that are expected in early visual cortex for such perceptual choice tasks (e.g. [11,30]), we focused on the stimulus- and choice-specific frequency bands identified in previous analyses. Furthermore, we used hemisphere-averaged power values for neural activity kernels because we assumed that decision-related activity in visual cortex

would be distributed across both left and right parts of each visual field map. This assumption was motivated by (i) the stimulus spanning both visual hemifields and (ii) correspondingly, sample contrast decoding being nearly identical for hemisphere averaged vs. separate-hemisphere signals (see previous section). Finally, we carried out a simple ROC-AUC analysis based on a single scalar variable, thus avoiding the need to fit free parameters for decoding this analysis. These choices made the analysis maximally similar to studies that computed choice probabilities of single neurons in primary visual cortex [11,30] and maximally sensitive for small-amplitude choice-predictive signals.

We used hemisphere-averaged gamma-band (collapsed across center frequencies 50-65 Hz, i.e., bandwith: 40-75 Hz; compare with Figure 2B) or low-frequency band (center frequency: 10 Hz, bandwith: 0-20 Hz) power values extracted from visual cortical field maps for each sample position *i* (at t=190 ms after sample onset, i.e. average peak contrast encoding of individual samples) to compute ROC-AUC values. The so-computed kernels are referred to as "overall" kernels in Figure 4.

A follow-up analysis aimed to further remove the effect of trial-to-trial fluctuations of the external contrast samples and isolate choice-predictive activity originating from intrinsic sources. Here, we regressed single-trial sample contrast values on the corresponding cortical power values (again at t=190 ms after sample onset). We then subtracted this prediction from power values and used these residuals in the computation of V1 kernels, yielding the so-called "residual" kernels in Figure 4.

For the cross-correlation with M1 choice decoding time courses (see next section), we also re-computed "overall" low-frequency kernels at the same (higher) temporal resolution (Figure S10 for V1) as used for choice decoding in Figure 2. To this end, we computed ROC-AUC values for each time-point *t*.

Logistic regression of alpha- and gamma-band activity on choice

To complement the above neural-activity kernel analysis, we used logistic regression to model single-trial choice as a function of visual gamma-band (bandwidth 40-75 Hz) and low-frequency band (bandwidth 0-20 Hz) power and, importantly, their interaction. The interaction term in this model assessed the extent to which fluctuations in low-frequency power altered the relationship between gamma-band power and choice. We first averaged power values at each frequency band (again at 190 ms post-sample onset) over the first (samples 1-5) and second (samples 6-10) half of contrast samples per trial, with the aim of mitigating noise in the single-sample responses but preserving our ability to assess temporal asymmetries between frequency bands. For each visual field map ROI, we then fit the following regression model:

$$y_{trl} = logistic\left[\sum_{h\in\{1,2\}} \beta_{1,h}\alpha_{trl,h} + \beta_{2,h}\gamma_{trl,h} + \beta_{3,h}\alpha_{trl,h}\gamma_{trl,h} + \beta_0\right], \qquad (9)$$

where y denotes single-trial choice, α and γ denote (z-scored) low-frequency and gamma-band activity, respectively, and h denotes the trial half. We assessed the group-level significance of individual terms from this choice model via one-sample t-test against zero, computed temporal asymmetry scores by subtracting $\beta_{n,1}$ from $\beta_{n,2}$, and tested for differences in these temporal asymmetries between the two frequency bands via paired-samples t-test (Figure S9).

Cross-correlation of choice-predictive activity in M1 and visual cortical low-frequency kernels

We aimed to quantify the association between the time course of choice-predictive activity in M1-hand and low-frequency kernels in all visual cortical field maps. To this end, we computed, for each subject, the cross-correlation between the M1-hand choice decoding time course (ROC-AUC values from) and the high temporal resolution version of low-frequency kernels. Specifically, for each visual field map, we computed the Pearson correlation between the ROC-AUC values from M1-hand in the interval from *t=0* to *t=0.8* s and time-shifted versions (lags from -215 to 215 ms) of the low-frequency kernel for that visual field map (Figure 5, inset). A lag of 100 ms, for example, correlated M1-hand ROC-AUC values in the interval *t=[0,0.8] s* with low-frequency kernels in the interval *t=[0.1, 0.9] s*. This analysis yielded one correlation coefficient per lag, subject and visual field map. The cross-correlation functions for all visual field maps were finally collapsed, and tested for significance, across subjects (Figure 5). Positive lags of the peak cross-correlation indicated a temporal advance of choice decoding performance in M1-

hand ("M1 leads"). Negative lags of the peak cross-correlation indicated an advance of the low-frequency kernels in visual field maps (e.g. "V1 leads").

Signal leakage between ROIs can confound correlations between estimates of regionally specific activity derived from source-reconstructed MEG-data [94]. Such leakage can occur due genuine field spread (volume conduction) as well as the limited precision of the LCMV spatial filters. To obtain an upper bound of the effect of signal leakage present in our data, we computed the zero-lag correlation between the ROC-AUC values of the M1-hand choice decoder and the low-frequency kernel, now taken from M1-hand, rather than the visual field maps. Because this zero-lag correlation it compared two (partially redundant) signals obtained from the exact same ROI, it quantified the maximum possible leakage effects in our data. Thus, we used it as a conservative "reference correlation" (Figure 5, green) against which we compared the cross-correlation values obtained for the visual field maps (paired t-tests). Any significant difference pinpointed a component of visual field map cross-correlations that was unconfounded by signal leakage.

The low-frequency kernels were based on spectral estimates for 0-20 Hz activity and the choice decoder time courses were based on mixtures of different frequencies (1-145 Hz), which were partially computed with different time windows (longer for frequencies < 10 Hz, see section *Preprocessing, Spectral analysis, and Source Reconstruction of MEG Data*). Another concern about the cross-correlation analysis might be that these signal processing differences might induce artefactual time shifts in the cross-correlation functions (e.g. due to power changes in one band being detected earlier than in the other). This concern might render the peak lags observed in Figure 5 difficult to interpret functionally. We ruled out this concern by systematically simulating cross-correlations of pairs of oscillatory signals with various different characteristics (transient vs. sustained vs. ramping power increases, pure vs. noisy oscillations) and then analyzed the signals in the exact same way as our actual MEG data (multi-taper sliding window FFT followed by cross-correlation as described above). We observed much higher positive lags in the data than in any of these simulations (Figure S11). This renders it highly unlikely that the peak lags reported in Figure 5 were caused by signal processing artefacts.

Specifically, for each scenario, we simulated (250 simulation runs per scenario) a 10 Hz "reference" signal" and a "comparison" signal of varying frequency (e.g., 50 Hz, Figure S11A). For sustained power increases of both signals at the same point *t=0* the cross-correlation of power time-course showed no induced time-delays for $F \geq 10$ and negative delays in the order of -25 to -50 ms for $F < 10$ Hz (Figure S11A). For two transient signals (single cycle) we found a positive lag of 40 ms (Figure S11B, C), because the detection of the power increase differed: The power increase in the 10 Hz signal was maximal when the time-window used for power computation was centered on the peak of the transient 10 Hz signal, i.e. after 50 ms (half of a 10 Hz cycle); the power increase of the 50 Hz cycle was maximal after 10 ms (half of a 50 Hz cycle). This yielded 40 ms as the difference between the two half-cycle durations. Other frequency combinations ($F \geq 10$ Hz) produced a delay of $0.05 - \frac{1}{2F}$ s, which was bounded by 50 ms. Even this lag was substantially shorter than the peak lag observed in the data for early visual cortex (areas V1-V4, Figure 5). Further comparison frequencies < 10 Hz used two different time windows for power computation (as we did for the MEG data analysis) yielded negative delays, opposite to what we found in the data (Figure 5). For the (more realistic) up-ramping signals (linear ramps, Figure S11D, E) we obtained results in between those for sustained and transient signals, with small (<25 ms) absolute values of the peak lags (Figure S11D, E).

The code for all analysis steps is available at https://github.com/DonnerLab/2020_Large-scale-Dynamics-of-Perceptual-Decision-Information-across-Human-Cortex.

Data Availability

The source data underlying all figures are provided with the paper. Source-reconstructed MEG data will be made publicly available upon publication. Raw MEG data will be made available upon request.

References

1. Bogacz, R., Brown, E., Moehlis, J., Holmes, P. & Cohen, J. D. The physics of optimal decision making: A formal analysis of models of performance in two-alternative forced-choice tasks. Psychol. Rev. 113, 700–765 (2006).
2. Gold, J. I. & Shadlen, M. N. The neural basis of decision making. Annu. Rev. Neurosci. 30, 535–74 (2007).
3. Yang, T. & Shadlen, M. N. Probabilistic reasoning by neurons. Nature 447, 1075–1080 (2007).
4. Brunton, B. W., Botvinick, M. M. & Brody, C. D. Rats and Humans Can Optimally Accumulate Evidence for Decision-Making. Science 340, 95–98 (2013).
5. Ratcliff, R. & McKoon, G. The Diffusion Decision Model: Theory and Data for Two-Choice Decision Tasks. Neural Comput. 20, 873–922 (2008).
6. Shadlen, M. N. & Kiani, R. Decision making as a window on cognition. Neuron 80, 791–806 (2013).
7. Kepecs, A., Uchida, N., Zariwala, H. a & Mainen, Z. F. Neural correlates, computation and behavioural impact of decision confidence. Nature 455, 227–231 (2008).
8. Sanders, J. I., Hangya, B. & Kepecs, A. Signatures of a Statistical Computation in the Human Sense of Confidence. Neuron 90, 499–506 (2016).
9. Kiani, R. & Shadlen, M. N. Representation of confidence associated with a decision by neurons in the parietal cortex. Science 324, 759–764 (2009).
10. Gold, J. I. & Shadlen, M. N. Neural computations that underlie decisions about sensory stimuli. Trends Cogn. Sci. 5, 10–16 (2001).
11. Britten, K. H., Newsome, W. T., Shadlen, M. N., Celebrini, S. & Movshon, J. A. A relationship between behavioral choice and the visual responses of neurons in macaque MT. Vis. Neurosci. 13, 87–100 (1996).
12. Siegel, M., Buschman, T. J. & Miller, E. K. Cortical information flow during flexible sensorimotor decisions. 348, 1352–1356 (2015).
13. Hanks, T. D. et al. Distinct relationships of parietal and prefrontal cortices to evidence accumulation. Nature 520, 220–223 (2015).
14. Mante, V., Sussillo, D., Shenoy, K. V. & Newsome, W. T. Context-dependent computation by recurrent dynamics in prefrontal cortex. Nature 503, 78–84 (2013).
15. Donner, T. H., Siegel, M., Fries, P. & Engel, A. K. Buildup of choice-predictive activity in human motor cortex during perceptual decision making. Curr. Biol. 19, 1581–5 (2009).
16. O'Connell, R. G., Dockree, P. M. & Kelly, S. P. A supramodal accumulation-to-bound signal that determines perceptual decisions in humans. Nat. Neurosci. 15, 1729–1735 (2012).
17. Wyart, V., de Gardelle, V., Scholl, J. & Summerfield, C. Rhythmic Fluctuations in Evidence Accumulation during Decision Making in the Human Brain. Neuron 76, 847–858 (2012).
18. Fischer, A. G., Nigbur, R., Klein, T. A., Danielmeier, C. & Ullsperger, M. Cortical beta power reflects decision dynamics and uncovers multiple facets of post-error adaptation. Nat. Commun. 9, 5038 (2018).
19. Brody, C. D. & Hanks, T. D. Neural underpinnings of the evidence accumulator. Curr. Opin. Neurobiol. 37, 149–157 (2016).
20. Mazurek, M. E., Roitman, J. D., Ditterich, J. & Shadlen, M. N. A Role for Neural Integrators in Perceptual Decision Making. Cereb. Cortex 13, 1257–1269 (2003).
21. Hernández, A. et al. Decoding a Perceptual Decision Process across Cortex. Neuron 66, 300–314 (2010).
22. Yates, J. L., Park, I. M., Katz, L. N., Pillow, J. W. & Huk, A. C. Functional dissection of signal and noise in MT and LIP during decision-making. Nat. Neurosci. 20, 1285–1292 (2017).
23. Pinto, L. et al. Task-Dependent Changes in the Large-Scale Dynamics and Necessity of Cortical Regions. Neuron 104, 810-824.e9 (2019).
24. Cumming, B. G. & Nienborg, H. Feedforward and feedback sources of choice probability in neural population responses. Curr. Opin. Neurobiol. 37, 126–132 (2016).

25. Wimmer, K. et al. Sensory integration dynamics in a hierarchical network explains choice probabilities in cortical area MT. Nat. Commun. 6, 6177 (2015).
26. Haefner, R. M., Berkes, P. & Fiser, J. Perceptual decision-making as probabilistic inference by sampling. Neuron 90, 649–660 (2016).
27. Shadlen, M., Britten, K., Newsome, W. & Movshon, J. A computational analysis of the relationship between neuronal and behavioral responses to visual motion. J. Neurosci. 16, 1486–1510 (1996).
28. Felleman, D. J. & Van Essen, D. C. Distributed hierarchical processing in the primate cerebral cortex. Cereb. Cortex 1, 1–47 (1991).
29. Markov, N. T. et al. Anatomy of hierarchy: feedforward and feedback pathways in macaque visual cortex. J. Comp. Neurol. 522, 225–59 (2014).
30. Nienborg, H. & Cumming, B. G. Decision-related activity in sensory neurons reflects more than a neuron's causal effect. Nature 459, 89–92 (2009).
31. Bondy, A. G., Haefner, R. M. & Cumming, B. G. Feedback determines the structure of correlated variability in primary visual cortex. Nat. Neurosci. 21, 598–606 (2018).
32. Macke, J. H. & Nienborg, H. Choice (-history) correlations in sensory cortex: cause or consequence? Curr. Opin. Neurobiol. 58, 148–154 (2019).
33. Urai, A. E., Braun, A. & Donner, T. H. Pupil-linked arousal is driven by decision uncertainty and alters serial choice bias. Nat. Commun. 8, 14637 (2017).
34. Kiani, R., Hanks, T. D. & Shadlen, M. N. Bounded integration in parietal cortex underlies decisions even when viewing duration is dictated by the environment. J. Neurosci. Off. J. Soc. Neurosci. 28, 3017–3029 (2008).
35. Zylberberg, A., Barttfeld, P. & Sigman, M. The construction of confidence in a perceptual decision. Front. Integr. Neurosci. 6, 1–10 (2012).
36. Okazawa, G., Sha, L., Purcell, B. A. & Kiani, R. Psychophysical reverse correlation reflects both sensory and decision-making processes. Nat. Commun. 9, (2018).
37. Green, D. M. & Swets, J. A. Signal detection theory and psychophysics. (Jon Wiley & Sons, Inc., 1966).
38. Tsetsos, K., Gao, J., McClelland, J. L. & Usher, M. Using Time-Varying Evidence to Test Models of Decision Dynamics: Bounded Diffusion vs. the Leaky Competing Accumulator Model. Front. Neurosci. 6, (2012).
39. Michalareas, G. et al. Alpha-Beta and Gamma Rhythms Subserve Feedback and Feedforward Influences among Human Visual Cortical Areas. Neuron 89, 384–397 (2016).
40. Hadjipapas, A., Lowet, E., Roberts, M. J., Peter, A. & De Weerd, P. Parametric variation of gamma frequency and power with luminance contrast: A comparative study of human MEG and monkey LFP and spike responses. NeuroImage 112, 327–340 (2015).
41. Ray, S. & Maunsell, J. H. R. Differences in Gamma Frequencies across Visual Cortex Restrict Their Possible Use in Computation. Neuron 67, 885–896 (2010).
42. Hoogenboom, N., Schoffelen, J.-M., Oostenveld, R., Parkes, L. M. & Fries, P. Localizing human visual gamma-band activity in frequency, time and space. NeuroImage 29, 764–773 (2006).
43. Hall, S. D. et al. The missing link: analogous human and primate cortical gamma oscillations. NeuroImage 26, 13–17 (2005).
44. Henrie, J. A. & Shapley, R. LFP Power Spectra in V1 Cortex: The Graded Effect of Stimulus Contrast. J. Neurophysiol. 94, 479–490 (2005).
45. Donner, T. H. & Siegel, M. A framework for local cortical oscillation patterns. Trends Cogn. Sci. 15, 191–199 (2011).
46. Gardner, J. L. et al. Contrast adaptation and representation in human early visual cortex. Neuron 47, 607–20 (2005).
47. Dehaene, S. et al. Inferring behavior from functional brain images. Nat. Neurosci. 1, 549–549 (1998).
48. de Gee, J. W. et al. Dynamic modulation of decision biases by brainstem arousal systems. eLife 6, 1–36 (2017).
49. de Lange, F. P., Rahnev, D. a, Donner, T. H. & Lau, H. Prestimulus oscillatory activity over motor cortex reflects perceptual expectations. J. Neurosci. 33, 1400–10 (2013).
50. de Lafuente, V. & Romo, R. Neural correlate of subjective sensory experience gradually builds up across cortical areas. Proc. Natl. Acad. Sci. 103, 14266–14271 (2006).

51. Latimer, K. W., Yates, J. L., Meister, M. L. R., Huk, A. C. & Pillow, J. W. Single-trial spike trains in parietal cortex reveal discrete steps during decision-making. Science 349, 184–187 (2015).
52. Katz, L. N., Yates, J. L., Pillow, J. W. & Huk, A. C. Dissociated functional significance of decision-related activity in the primate dorsal stream. Nature 535, 285–288 (2016).
53. Ball, T., Schulze-Bonhage, A., Aertsen, A. & Mehring, C. Differential representation of arm movement direction in relation to cortical anatomy and function. J. Neural Eng. 6, 016006 (2009).
54. Kamitani, Y. & Tong, F. Decoding the visual and subjective contents of the human brain. Nat. Neurosci. 8, 679–85 (2005).
55. Haynes, J.-D. & Rees, G. Predicting the orientation of invisible stimuli from activity in human primary visual cortex. Nat. Neurosci. 5, 221–221 (2005).
56. Hebart, M. N., Schriever, Y., Donner, T. H. & Haynes, J.-D. The Relationship between Perceptual Decision Variables and Confidence in the Human Brain. Cereb. Cortex 26, 118–130 (2014).
57. Kok, P., Jehee, J. F. M. & de Lange, F. P. Less Is More: Expectation Sharpens Representations in the Primary Visual Cortex. Neuron 75, 265–270 (2012).
58. Cichy, R. M., Pantazis, D. & Oliva, A. Resolving human object recognition in space and time. Nat. Neurosci. 17, 1–10 (2014).
59. King, J.-R. & Dehaene, S. Characterizing the dynamics of mental representations: the temporal generalization method. Trends Cogn. Sci. 18, 203–210 (2014).
60. Mostert, P., Kok, P. & de Lange, F. P. Dissociating sensory from decision processes in human perceptual decision making. Sci. Rep. 5, 18253 (2015).
61. Guo, Z. V. et al. Flow of Cortical Activity Underlying a Tactile Decision in Mice. Neuron 81, 179–194 (2014).
62. Hebart, M. N., Donner, T. H. & Haynes, J.-D. Human visual and parietal cortex encode visual choices independent of motor plans. NeuroImage 63, 1393–1403 (2012).
63. Gold, J. I. & Shadlen, M. N. The Influence of Behavioral Context on the Representation of a Perceptual Decision in Developing Oculomotor Commands. J. Neurosci. 23, 632–651 (2003).
64. Panzeri, S., Harvey, C. D., Piasini, E., Latham, P. E. & Fellin, T. Cracking the Neural Code for Sensory Perception by Combining Statistics, Intervention, and Behavior. Neuron 93, 491–507 (2017).
65. Logothetis, N. K., Pauls, J., Augath, M., Trinath, T. & Oeltermann, A. Neurophysiological investigation of the basis of the fMRI signal. Nature 412, 150–157 (2001).
66. Heeger, D. J., Huk, A. C., Geisler, W. S. & Albrecht, D. G. Spikes versus BOLD: what does neuroimaging tell us about neuronal activity? Nat. Neurosci. 3, 631–633 (2000).
67. Siegel, M., Donner, T. H., Oostenveld, R., Fries, P. & Engel, A. K. High-Frequency Activity in Human Visual Cortex Is Modulated by Visual Motion Strength. Cereb. Cortex 17, 732–741 (2007).
68. Chicharro, D., Panzeri, S. & Haefner, R. M. Stimulus dependent relationships between behavioral choice and sensory neural responses. (2019) doi:10.1101/2019.12.27.889550.
69. Jensen, O. & Colgin, L. L. Cross-frequency coupling between neuronal oscillations. Trends Cogn. Sci. 11, 267–269 (2007).
70. Krekelberg, B., Boynton, G. M. & van Wezel, R. J. A. Adaptation: from single cells to BOLD signals. Trends Neurosci. 29, 250–256 (2006).
71. Kohn, A. Visual Adaptation: Physiology, Mechanisms, and Functional Benefits. J. Neurophysiol. 97, 3155–3164 (2007).
72. Buffalo, E. A., Fries, P., Landman, R., Buschman, T. J. & Desimone, R. Laminar differences in gamma and alpha coherence in the ventral stream. Proc. Natl. Acad. Sci. 108, 11262–11267 (2011).
73. Bastos, A. M. et al. Visual Areas Exert Feedforward and Feedback Influences through Distinct Frequency Channels. Neuron 85, 390–401 (2015).
74. Mejias, J. F., Murray, J. D., Kennedy, H. & Wang, X.-J. Feedforward and feedback frequency-dependent interactions in a large-scale laminar network of the primate cortex. Sci. Adv. 2, e1601335 (2016).
75. van Kerkoerle, T. et al. Alpha and gamma oscillations characterize feedback and feedforward processing in monkey visual cortex. Proc. Natl. Acad. Sci. 111, 14332–14341 (2014).
76. Spaak, E., Bonnefond, M., Maier, A., Leopold, D. A. & Jensen, O. Layer-Specific Entrainment of Gamma-Band Neural Activity by the Alpha Rhythm in Monkey Visual Cortex. Curr. Biol. 22, 2313–2318 (2012).
77. Fries, P. Rhythms for Cognition: Communication through Coherence. Neuron 88, 220–235 (2015).

78. Bastos, A. M. et al. Canonical microcircuits for predictive coding. Neuron 76, 695–711 (2012).
79. Murphy, P. R., Wilming, N., Hernandez-Bocanegra, D. C., Ortega, G. P. & Donner, T. H. Normative Circuit Dynamics Across Human Cortex During Evidence Accumulation in Changing Environments. http://biorxiv.org/lookup/doi/10.1101/2020.01.29.924795 (2020) doi:10.1101/2020.01.29.924795.
80. Talluri, B. C., Urai, A. E., Tsetsos, K., Usher, M. & Donner, T. H. Confirmation Bias through Selective Overweighting of Choice-Consistent Evidence. Curr. Biol. 28, 3128-3135.e8 (2018).
81. Yu, A. J. & Dayan, P. Uncertainty, neuromodulation, and attention. Neuron 46, 681–692 (2005).
82. Nassar, M. R. et al. Rational regulation of learning dynamics by pupil-linked arousal systems. Nat. Neurosci. 15, 1040–6 (2012).
83. Mathys, C. D. et al. Uncertainty in perception and the Hierarchical Gaussian Filter. Front. Hum. Neurosci. 8, 825 (2014).
84. Glaze, C. M., Kable, J. W. & Gold, J. I. Normative evidence accumulation in unpredictable environments. eLife 4, (2015).
85. Watson, A. B. & Pelli, D. G. Quest: A Bayesian adaptive psychometric method. Percept. Psychophys. 33, 113–120 (1983).
86. Van Veen, B. D., Van Drongelen, W., Yuchtman, M. & Suzuki, A. Localization of brain electrical activity via linearly constrained minimum variance spatial filtering. IEEE Trans. Biomed. Eng. 44, 867–880 (1997).
87. Oostenveld, R., Fries, P., Maris, E. & Schoffelen, J.-M. FieldTrip: Open Source Software for Advanced Analysis of MEG, EEG, and Invasive Electrophysiological Data. Comput. Intell. Neurosci. 2011, 1–9 (2011).
88. Gramfort, A. et al. MNE software for processing MEG and EEG data. NeuroImage 86, 446–460 (2014).
89. Wang, L., Mruczek, R. E. B., Arcaro, M. J. & Kastner, S. Probabilistic Maps of Visual Topography in Human Cortex. Cereb. Cortex 25, 3911–3931 (2015).
90. Glasser, M. F. et al. A multi-modal parcellation of human cerebral cortex. Nature 536, 171–178 (2016).
91. Wandell, B. a, Dumoulin, S. O. & Brewer, A. a. Visual field maps in human cortex. Neuron 56, 366–83 (2007).
92. Bishop, C. M. Pattern Recognition and Machine Learning. vol. 16 (Springer, 2008).
93. Salvatier, J., Wiecki, T. V. & Fonnesbeck, C. Probabilistic programming in Python using PyMC3. PeerJ Comput. Sci. 2, e55 (2016).
94. Siegel, M., Donner, T. H., & Engel A. K. Spectral fingerprints of large-scale neuronal interactions. Nature Reviews Neuroscience. 13, 121-134 (2012).

Supplementary Figures: Large-scale Dynamics of Perceptual Decision Information across Human Cortex

Niklas Wilming, Peter R Murphy, Florent Meyniel, Tobias H Donner

Figure S1. Relationships between sensory evidence, choice accuracy, and confidence.

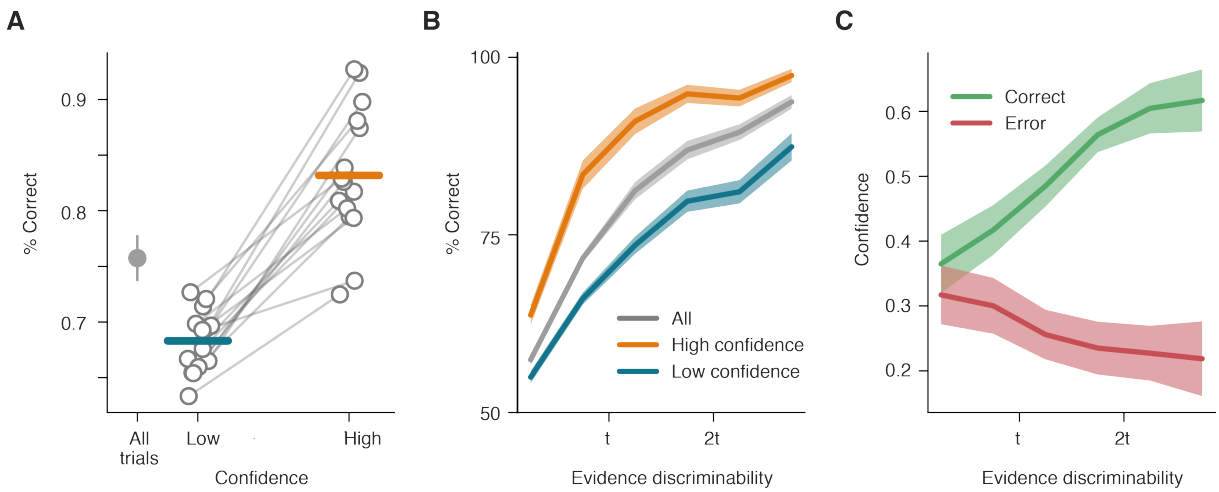

A. Choice accuracy, overall and split by participants' confidence reports (high vs. low). Lines, individual participants. Dots, group average (error bars, s.e.m.); lines, individual participants. **B.** Choice accuracy as function of evidence strength in units of threshold (1t = 75% correct; determined by QUEST staircase). Black/gray, overall dependency; colors, dependence split by confidence; lines, group average; shaded regions, s.e.m. **C.** Probability of high confidence report as function of evidence strength, separately for correct and erroneous choices. Taken together, participants' behavioral choices and confidence reports exhibited a lawful dependence on external evidence strength. Specifically, confidence reports revealed three signatures of a measure of statistical decision confidence, defined as the probability of being correct, given the choice made and the evidence [1–3]: (i) accuracy was larger for high than low confidence (panel **A**); (ii) choice accuracy increased more rapidly as function of evidence strength for high than for low confidence (panel **B**); (iii) probability of high confidence reports increased as function of evidence strength on trials with correct choice, but decreased as function of evidence strength on error trials (panel **C**). Source data are provided as a Source Data file.

Figure S2: Baseline and task-related neural activity in different frequency bands.

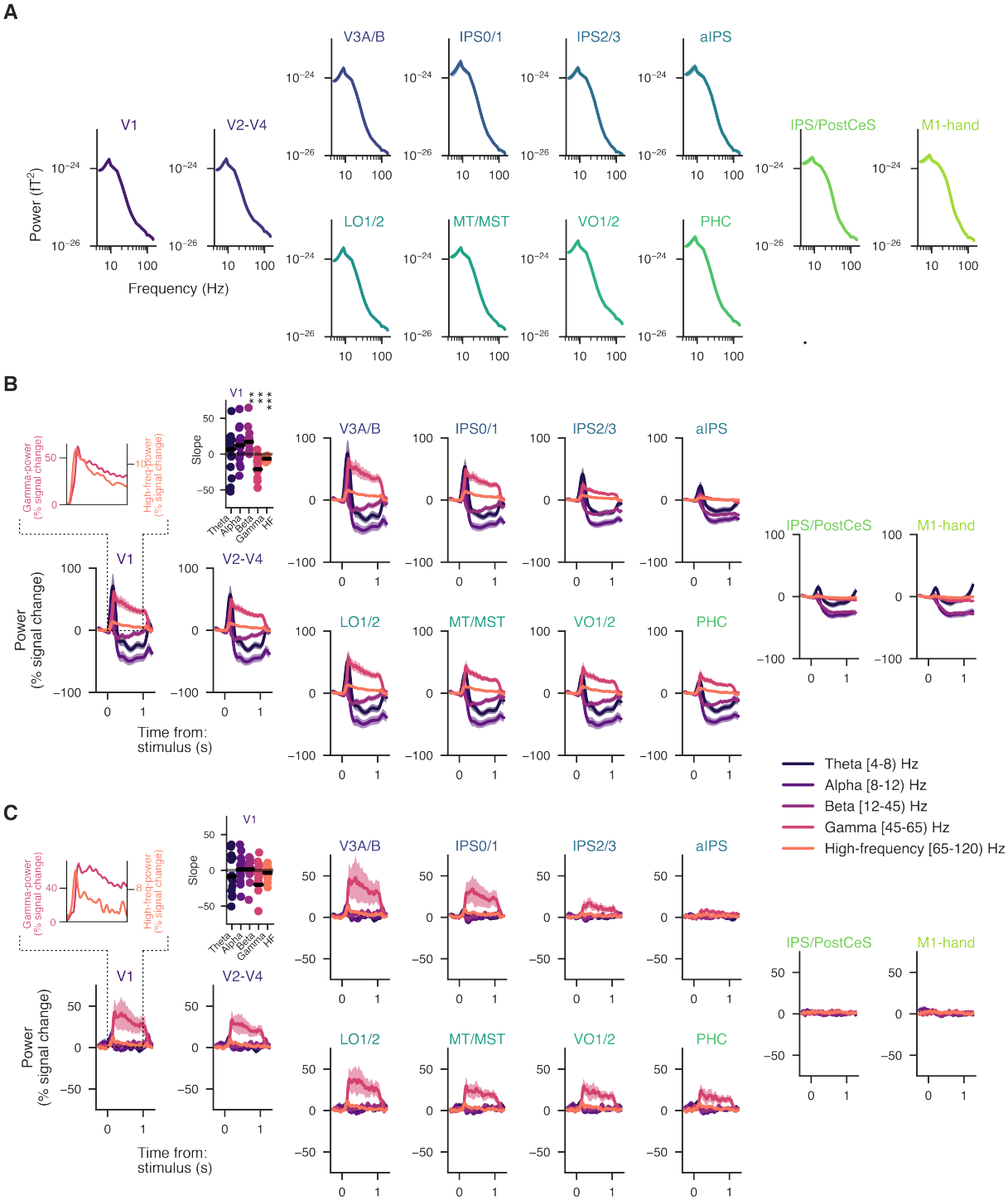

A. Pre-stimulus baseline power spectra for all cortical regions shown in main Figure 2. Dashed vertical lines indicate baseline period. **B.** Time course of change of band-limited power relative to baseline during the test stimulus presentation, for same cortical regions as in Figure 2. Frequency bands have been defined so as to span the full range of effects evident in our spectral analysis. Left inset (on top of V1), close-up of V1 power responses in the gamma-band and high-frequency band. Right inset, slope estimates (linear regression across interval 0.5 to 1s) for V1 power responses in different bands. **C.** As B, but now for the power response difference between stronger vs. weaker mean test contrast trials. *, $p < 0.05$; **, $p < 0.01$; ***, $p < 0{,}001$ (t-tests). Source data are provided as a Source Data file.

Figure S3: V1 gamma-band responses as function of contrast (sample) variance.

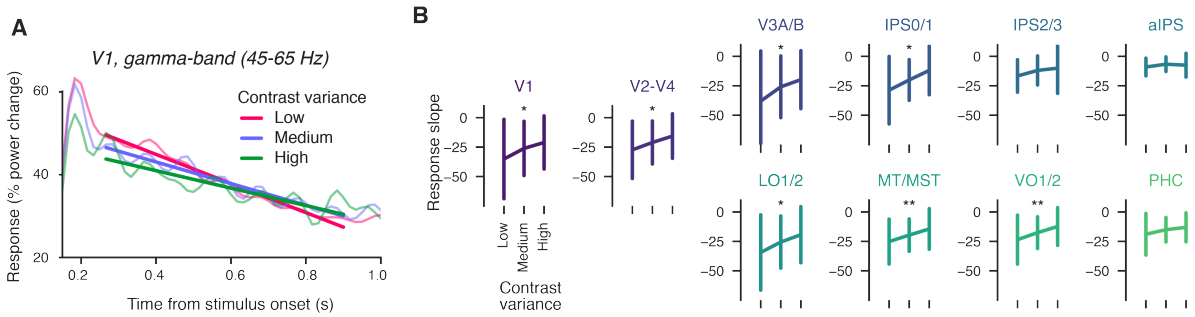

A. Time course of change of V1 gamma-band power relative to baseline during the test stimulus presentation, for three different levels of sample contrast variance during the test (equally spaced from minimum to maximum sample variance). Straight lines, fits of linear regressions for interval 265 to 900 ms from test stimulus onset, capturing the sustained response component exhibiting the linear down-ramp evident in Figure 2SB. **B.** Regression slopes as shown for V1 in panel A (+-SEM), for all visual cortical field maps, as function of sample variance (repeated measures ANOVA for factor sample variance; * = $p<0.05$, ** = $p<0.01$). Source data are provided as a Source Data file.

Figure S4: Correlation between psychophysical kernels band-power dynamics in V1.

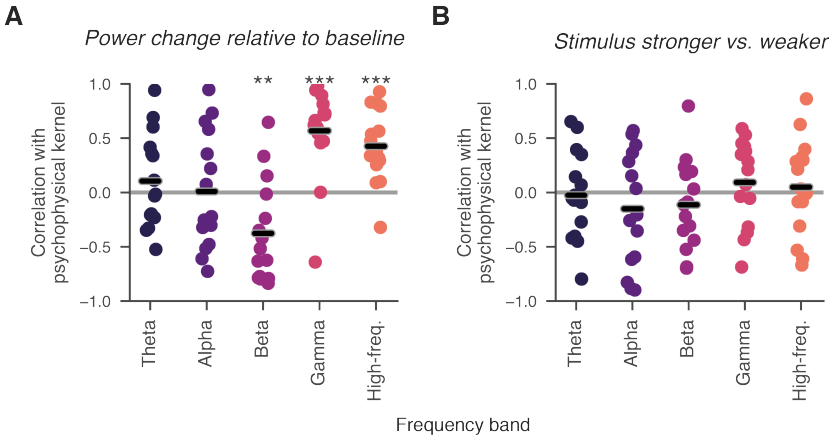

Temporal correlation between the band-power time courses of V1 from Figure S3 and the psychophysical kernels from Figure 1B. Each dot is one participant. Black lines, average correlation; *, $p < 0.05$; **, $p < 0.01$; ***, $p < 0.001$; two-sided t-tests. These correlations were computed excluding the first two samples so as to eliminate the non-specific onset transient response that spanned all frequency bands (see Figure S2B). Correlations were qualitatively identical for gamma- and high frequency-bands when including all samples, but then also significantly positive for theta- and alpha-bands, presumably driven by the onset transient followed by power-suppression. Source data are provided as a Source Data file.

Figure S5: Correlation between dynamics of band-power and contrast decoding in V1.

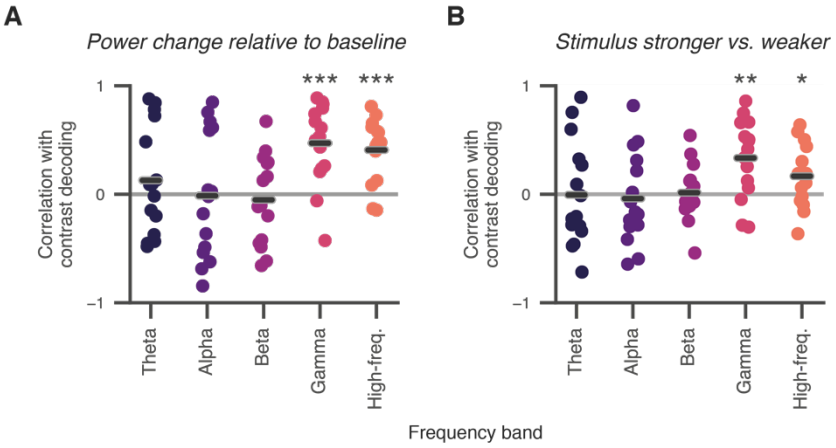

As Figure S3, but now correlating the band-power time courses to the V1 contrast decoding profiles from Figure 3B (left, orange line). Black lines, average correlation; *, $p < 0.05$; **, $p < 0.01$; ***, $p < 0.001$; two-sided t-tests. The individual temporal profiles of the decoding of momentary contrast samples in V1 (Figure 3B left, orange line) was strongly correlated with the profiles of the gamma-band and high-frequency responses. Thus, at least part of the decay evident in the contrast decoding profiles may be "inherited" from the decay of the underlying power responses (e.g., due to a decrease in signal-to-noise ratio for decoding). Source data are provided as a Source Data file.

Figure S6: Effector choice-related activity lateralization across visuo-motor pathway.

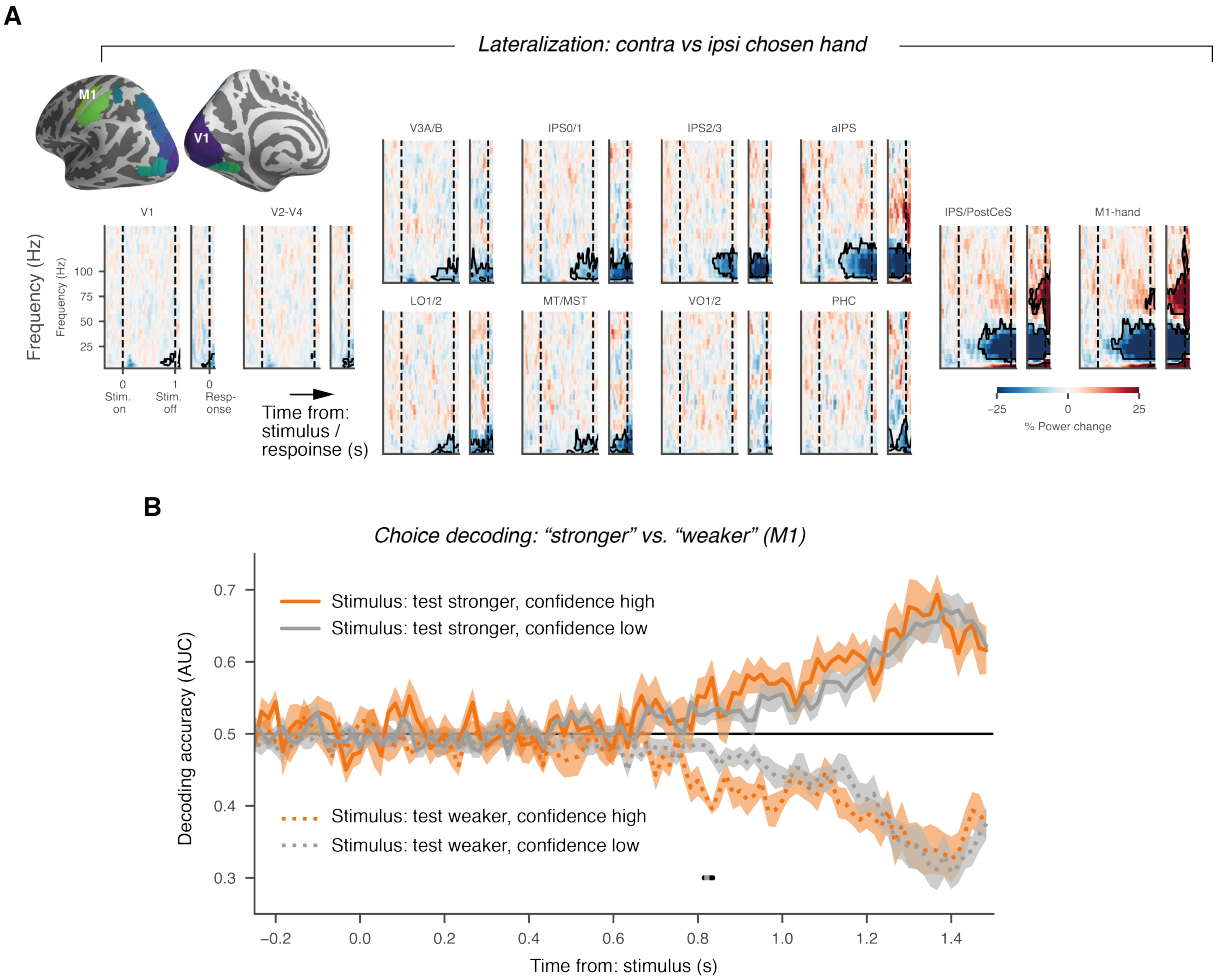

A. Time-frequency representations of power lateralization differences "test stronger" vs. "test weaker" choices. We subtracted power values contra-ipsilateral to the hand used for reporting the "test stronger" choice, and then contrasted lateralization values between "test stronger" and "test weaker" choices, separately for the two physical stimulus conditions (see Methods for details). Significant choice-related differential activity was evident before the motor response in three frequency bands, and most pronounced in the hand movement-selective ROIs M1-hand, IPS/PostCeS, and aIPS: low-frequency (< 8 Hz, contralateral increase), alpha/beta (8-40 Hz, contralateral suppression), and high gamma-band (50 – 100 Hz, contraleteral increase). Please note that choice-predictive alpha/beta-power lateralization in IPS/PostCeS and M1 became significant about 400 ms after stimulus onset, and then continued to build up throughout decision formation. **B.** Choice decoding, separately per stimulus category, as in Figure 2C, but now also sorted by the reported confidence level (high vs. low). Only 13 out the 15 participants could be used for this analysis because data needed to be sorted in a total of eight categories for this analysis and not enough trials were available for at least one of them (specifically, the high-confidence error trials) in the remaining participants. Source data are provided as a Source Data file.

Figure S7: Tracking choice-related neural dynamics across cortex.

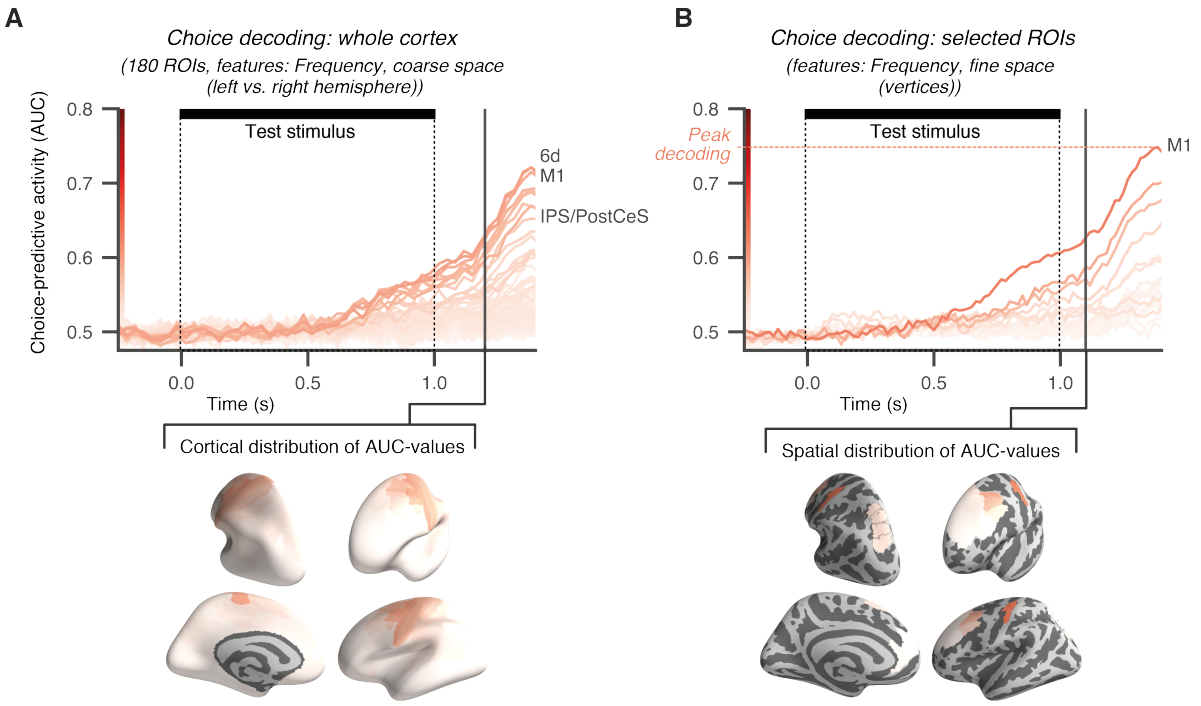

We used two alternatives to the choice-decoding approach used for Figure 2C (approach (i); Methods: *Decoding of choices*). **A.** Approach (ii): Time courses (top) and spatial distribution (bottom) of choice decoding accuracy (AUC, see main text) from 180 ROIs defined by Glasser et al [4]. Choice-decoding was performed separately per stimulus category, as in Figure 2C, and decoding AUC-scores were collapsed across categories, after flipping values about AUC-0.5. ROI-colors encode their AUC-values at t = 1.1s (black vertical line, see colorbar next to y-axis). Colors are displayed on inflated cortical surfaces in the bottom row. Strongest decoding performance at t=1.1 was found in three ROIs: dorsal premotor cortex (Brodman area 6d, AUC=0.595), M1 (Brodman area 4; AUC=0.59), and the frontal eye field (FEF; AUC FEF=0.59±0.02). Performance in these ROIs was indistinguishable (repeated measures ANOVA, t=1.1 s, $F(2,28)=0.42$, $p=0.66$). All other areas showed decoding performance smaller than M1-hand (paired t-test, $p<0.05$, uncorrected). **B.** Approach (iii): Time courses (top) and spatial distribution (bottom) of choice decoding accuracy (AUC) from M1-hand (for comparison) and 17 pre-selected ROIs covering dorsolateral prefrontal cortex anterior to premotor cortex. Here, we substantially increased the spatial granularity of the decoding approach by using spectral estimates from each vertex per ROI, and we also included spectral phase (in addition to spectral power) as features for decoding (Methods). Choice-decoding was performed independent of the stimulus category. Again, this showed maximum decoding performance for M1 (AUC=0.63). We found lower decoding performance for all dorsoalateral prefrontal ROIs tested (next best area, Brodman area i6-8 (premotor cortex): AUC=0.59, paired t-test: $p=0.002$, $t=-3.9$). Source data are provided as a Source Data file.

Figure S8: Residual alpha- and gamma-kernels across the visual hierarchy.

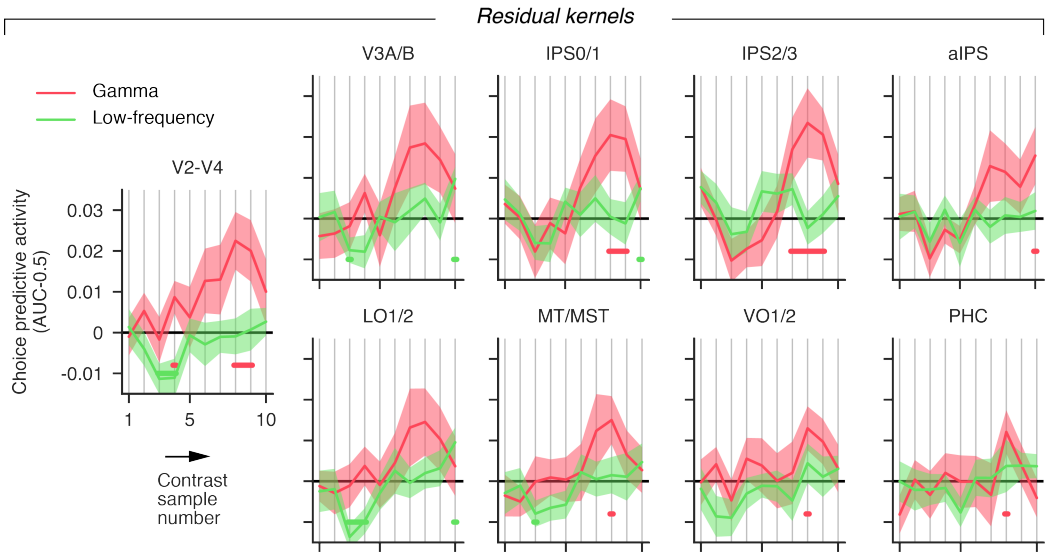

Residual choice-predictive activity (after removing external contrast fluctuations, see main text) across the visual cortical hierarchy. Residual kernels for low and gamma frequency-bands, as in main Figure 4A, but for extrastriate visual cortical field maps. Note the significant choice-predictive residual gamma-band activity on last sample for V3A/B, IPS1/2, and LO1/2. Source data are provided as a Source Data file.

Figure S9. Logistic regression of alpha- and gamma-power on behavioral choice.

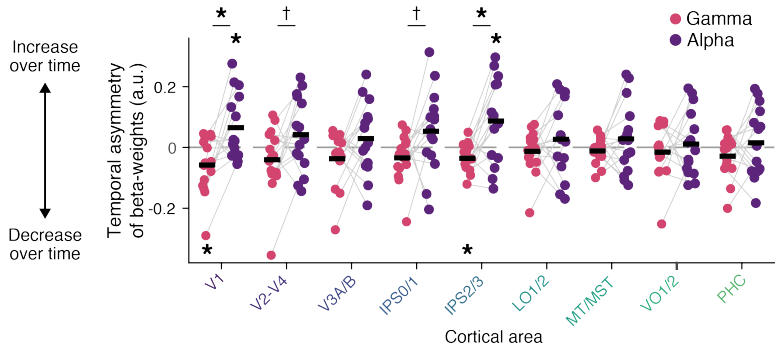

Temporal pattern (first vs. second half of test stimulus interval, within a trial) of gamma- and alpha-band activity on choice, for all visual field maps. *, $p < 0.05$; †, $p < 0.1$ (t-tests). Source data are provided as a Source Data file.

Figure S10. Group average V1 low-frequency kernel at higher temporal resolution.

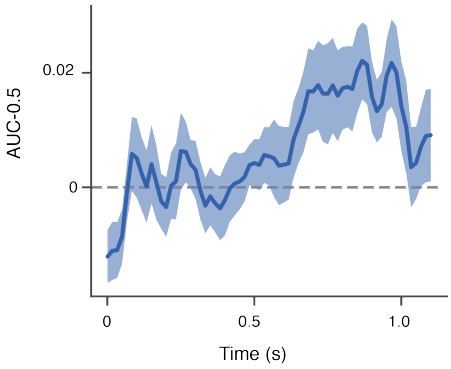

For cross-correlations with choice-specific signals in M1, the V1 low-frequency kernels (overall) as in main Figure 4A were recomputed at the same temporal resolution as the M1 choice decoding time courses from Figure 2C. Shaded area, SEM. Source data are provided as a Source Data file.

Figure S11. Simulation signal-processing induced coupling delays.

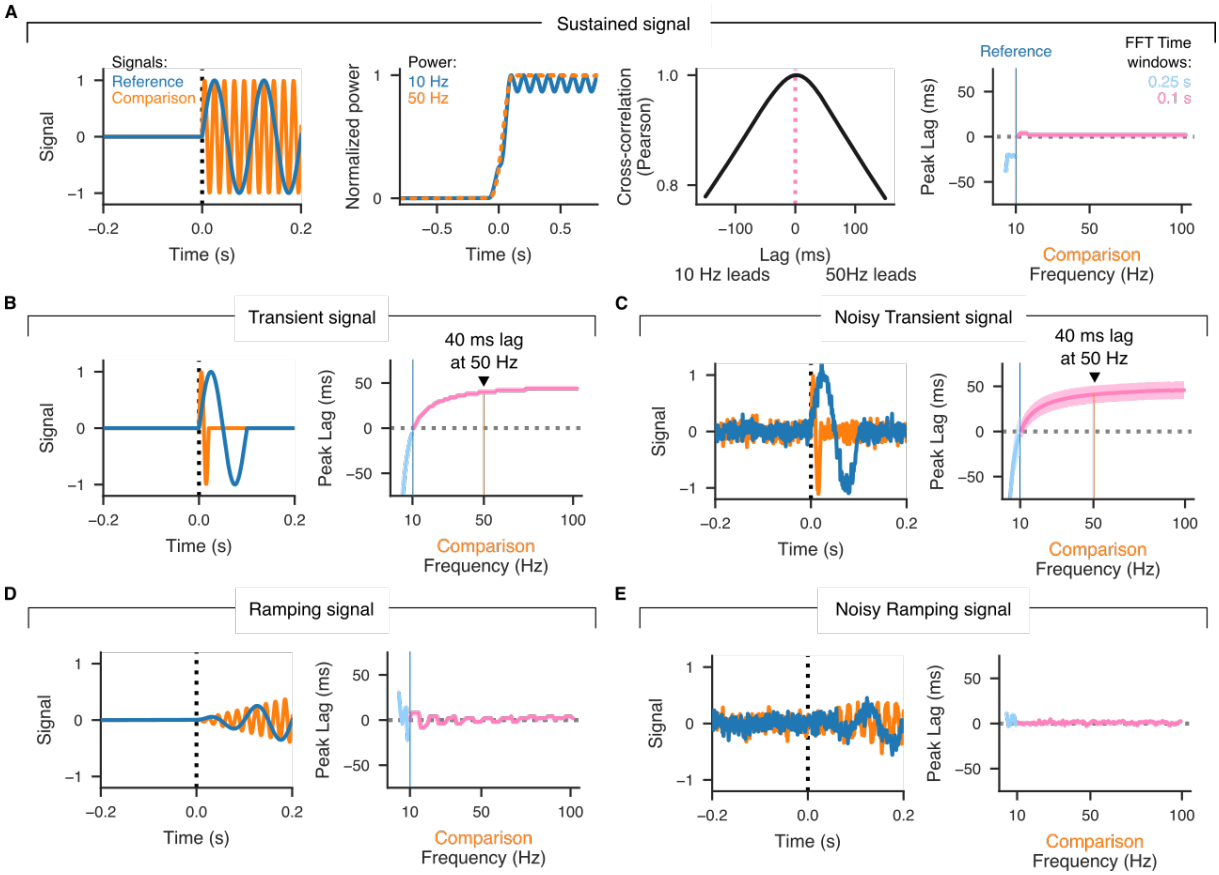

A. Schematic of simulation procedure (see also Methods). A sustained signal oscillating at 10 Hz ($y_r = \{^{sin(10*2\pi t)\ if\ \ t\geq 0}_{0,\ otherwise}$, 1000 Hz sampling frequency; 2 s duration; "reference" in left panel) starts concurrently with a signal oscillating at 50 Hz ($y_r = \{^{sin(50*2\pi t)\ if\ \ t\geq 0}_{0,\ otherwise}$, "comparison" in left panel). Their respective power change over time is shown in the center left panel (normalized to maximum of one). We evaluated power time courses with the exact same parameters as used for MEG analysis (multi-taper FFT, 100 ms time window for $F \geq 10$ Hz, 250 ms time for $F < 10$ Hz). The cross-correlation between two signals yields a single peak (center right panel). Varying the frequency of the comparison signal shows how the induced peak-lag changes as a function of the frequency difference between both signals (right panel). **B, C**. Same as A, but reference and comparison signals are transient, comprising only a single cycle. Transient signals yield positive lags for larger comparison frequencies and negative lags for smaller comparison frequencies. **B.** Noise-free transient signals. **C.** Transient signals are corrupted by Gaussian noise ($\mu = 0, \sigma = 0.1$). **D, E.** Same as A, but reference and comparison signals are up-ramping linearly. Ramping signals yield positive lags for larger comparison frequencies and negative lags for smaller comparison frequencies **D.** Noise-free ramping signals. **E.** Noise-corrupted ramping signals (same noise as in D). Ramping signals yield results in between those for sustained and transient signals, with small (<25 ms) absolute values of the peak lags. In sum, peak lags in all these simulated scenarios are much smaller than the ones observed in the data (Figure 5). Shades, $\pm$ 1 s.d. of 250 simulation runs.

Supplementary References

1. Sanders, J. I., Hangya, B. & Kepecs, A. Signatures of a Statistical Computation in the Human Sense of Confidence. *Neuron* 90, 499–506 (2016).
2. Pouget, A., Drugowitsch, J. & Kepecs, A. Confidence and certainty: distinct probabilistic quantities for different goals. *Nat. Neurosci.* 19, 366–374 (2016).
3. Urai, A. E., Braun, A. & Donner, T. H. Pupil-linked arousal is driven by decision uncertainty and alters serial choice bias. *Nat. Commun.* 8, 14637 (2017).
4. Glasser, M. F. *et al.* A multi-modal parcellation of human cerebral cortex. *Nature* 536, 171–178 (2016).
5. Bang, D. & Fleming, S. M. Distinct encoding of decision confidence in human medial prefrontal cortex. *Proc. Natl. Acad. Sci.* 115, 6082–6087 (2018).